energy&fuels

pubs.acs.org/EF

Article

A Predictive Physico-chemical Model of Biochar Oxidation

Andrea Locaspi,[§] Paulo Debiagi,[§] Matteo Pelucchi, Christian Hasse, and Tiziano Faravelli*

Cite This: *Energy Fuels* 2021, 35, 14894−14912

Read Online

ACCESS | Metrics & More | Article Recommendations | Supporting Information

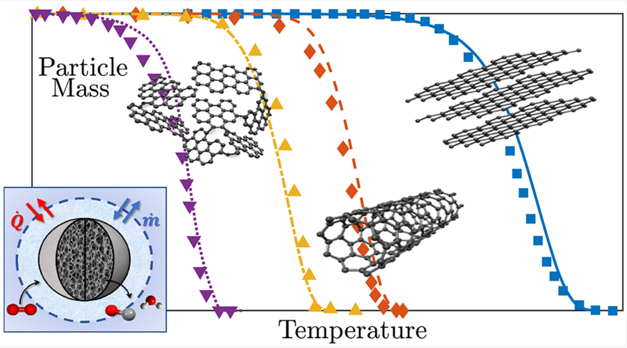

ABSTRACT: Pyrolysis of solid fuels forms a solid carbon-rich fuel, also called char, whose physico-chemical description is rather complex. Heterogeneous oxidation reactions take place during thermochemical conversion of char. The present work proposes a predictive detailed kinetic model, opening a new path for a deeper understanding of the char conversion process. This model considers porosity, surface area, density of surface sites, and their evolution along the conversion process. The chemical aspects of char oxidation are modeled assuming a carbonaceous bulk structure, surrounded by a variety of surface sites which represent the chemical functionalities typically present in such materials. The heterogeneous chemical reactions and their kinetic parameters are defined based on previous studies in the literature and by analogy to homogeneous gas-phase reactions of aromatic species. A mathematical framework is proposed to couple physical and chemical descriptions of the oxidation process. Although the proposed model benefits from experimental information, it is able to comprehensively describe the conversion rate of a broad range of carbonaceous materials such as carbon nanotubes, graphite, and chars only on the basis of their elemental composition. The proposed model represents a first step in exploring the explicit and coupled treatment given to the physical and chemical evolution of the fuel throughout its conversion, allowing us to consistently describe the particle evolution, opening a path for reliable models to manage the chemistry of char conversion.

1. INTRODUCTION

Biomass is increasingly being recognized as a promising carrier for heat, energy, and chemicals production. However, intense experimental and modeling research activities are necessary in order to improve the efficiency of industrial pyrolysis, combustion, and gasification reactors. Biomass combustion occurs in three main steps: pyrolysis, volatiles oxidation, and char oxidation.

Several models were proposed in the literature to describe the many facets of this problem. The large majority focused on the investigation of the pyrolysis step, proposing empirical or semi-empirical chemical reaction mechanisms which usually have a limited range of applications.[1−3] Other authors accomplished important improvements toward multi-component[4−6] and mechanistic pyrolysis models.[7,8] The available literature still lacks a comprehensive approach to describe the char conversion step, encompassing fuels that exhibit widely different physical and chemical characteristics. Studies on coal chars are broadly available, including a variety of experimental and modeling activities, but a comprehensive model is still missing. Beside some similarities, coal and biomass chars significantly differ in structural and compositional aspects which lead to different behaviors and properties in a reactive environment.[9,10]

Biochars are amorphous carbon structures containing residual amounts of oxygen and hydrogen, together with minor quantities of nitrogen and sulfur. Different quantities of ashes are also present in non-negligible amounts. The carbon content in char usually ranges between 65 and 95 wt%, depending on the initial biomass composition and pyrolysis operating conditions, while the hydrogen and oxygen content progressively drops as the pyrolysis temperature rises.[11,12] The content of H and O directly influences the rate of char conversion during oxidation and gasification.[13,14] Due to the large amounts of volatile matter present in biomass (usually around 60−85 wt%), the resulting biochars are significantly porous, thus strongly influencing the intrinsic surface area. This, combined with the high content of hydrogen and oxygen, results in a considerably higher reactivity in combustion/gasification conditions when compared with coal chars.[15,16]

In the past decades, several models were developed to describe oxidation of coal and biomass chars. The simplest empirical models consider a single *n*th order reaction, assuming a constant ratio of conversion of carbon into both CO and CO_2. These approaches are rather limited in their

Received: May 19, 2021
Revised: July 23, 2021
Published: September 1, 2021

https://doi.org/10.1021/acs.energyfuels.1c01559
Energy Fuels 2021, 35, 14894−14912

validity, as the selectivity of CO/CO_2 formation is very sensitive to the reaction temperature.[17] Models considering one reaction forming CO in competition with another reaction producing CO_2 overcome this issue, but the models remain fuel- and operation condition-specific.[18]

Models using Langmuir−Hinshelwood- or Elay−Rideal-based reaction mechanisms are widely used because of their improved physical description and capability to predict char conversion rates over wider ranges of temperature and pressure. Such models consider both the adsorption/desorption process in surface reaction kinetics and the physical evolution of the char particle, which strongly increases their comprehensiveness.

The most advanced char conversion models available consider a limited degree of complexity in chemical kinetics.[17−23] A more complex chemical description was formulated by Haynes and co-workers,[24,25] defining the concepts of turnover models for char oxidation, and explaining how surface reactions expose unreactive carbon to the gaseous environment. In this case the reactivity of different structures is described by means of a continuous distribution of activation energies. More recently, Tilghman and Mitchell[26] employed these concepts to develop an empirical semi-detailed model for gasification and combustion environments.

In the present work we use the state-of-the-art findings, briefly reiterated above, as the starting point for the proposed model. In order to focus on the reaction mechanism, experiments in kinetically controlled conditions, i.e., where both extra- and intra-particle diffusion characteristic times are shorter than the chemical kinetics, are preferentially used for validation of the model. Simple diffusion correlations were employed to describe the mass exchange with the environment. The novelty of the present work lies in the development of a comprehensive physico-chemical description of the particles' evolution. Literature models describing the particles' physical evolution are paired with a new detailed discrete reaction mechanism. The resulting coupling is able to consistently reproduce the complex evolution of the particles' chemical and physical properties during oxidation. The advantages of such a detailed approach are the capability to predictively describe the oxidation of a broad range of carbonaceous materials, requiring only the elemental composition and porosity of the initial fuel. No further information is required, even though the model takes advantage of specific measurements such as intrinsic surface area, density of surface sites, and skeletal density, when available.

2. PARTICLE MODELING

The present model considers a single particle of volume V_p in a constant control volume V. The system exchanges both heat and mass with a constant gaseous environment (ge), but thermal equilibrium is assumed at each time step between system and environment. Mass exchange is defined through a Fick diffusion flux (J) and a Darcy convective flux (D_f). The char particle is assumed spherical, and it is described similarly to heterogeneous catalysts.[27] The particle size is evaluated through a parameter γ with respect to the total volume, while the solid volume is determined through the void fraction ϵ. The total particle surface A_p is defined in terms of total particle volume through the volumetric specific surface S. A more in-depth description of the system, the evaluation of the mass fluxes, and the required parameters are reported in section S-I of the Supporting Information. A schematic representation of the system is reported in Figure 1a.

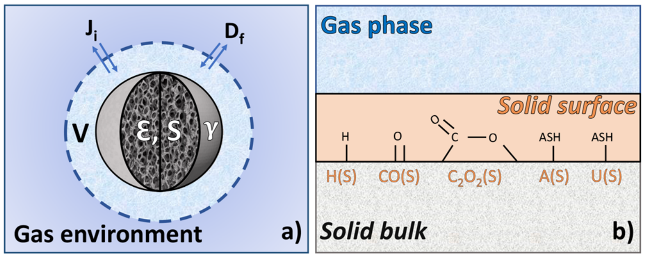

Figure 1. (a) Schematic description of the control volume V, with a particle of volume $V_p = \gamma V$, porosity ϵ, and volumetric specific surface area S. Mass exchange with the gas environment is represented through diffusive (J) and convective Darcy (D_f) fluxes. (b) Gas−solid interactions of the solid bulk region through the solid surface region described by the surface pseudo-species H(S), CO(S), C_2O_2(S), A(S), and U(S).

The solid particle is composed of a bulk region and a surface region. The solid surface is a monolayer described similarly to the active-site theory.[27] Several surface species are introduced to properly describe the conversion process. With respect to other models,[26,28,29] no free surface-site species is introduced. While the surface region interacts with the gas phase, the bulk region remains encapsulated by the surface. As the surface phase is consumed by the process, the bulk region is gradually exposed, becoming reactive to the gas phase. A schematic representation of these regions is illustrated in Figure 1b.

2.1. Chemical Characterization.

The char particle is composed of a substantial number of different chemical functionalities. In the present work, in order to reasonably describe the chemical moieties, a lumping approach is adopted[30,31] to introduce only a few solid-phase pseudo-species and their corresponding pseudo-reactions. Due to the char complex's 3D structure, the same functionalities may be both exposed to or hidden from the gas phase. For this reason, similar functionalities are introduced for both the surface and the bulk region. Table 1 summarizes the considered initial functionalities.

The initial surface layer is described by five pseudo-species. All surface hydrogen moieties are represented by a single surface pseudo-species H(S). Surface organic oxygen moieties are described by introducing the C_2O_2(S) and CO(S) pseudo-species, where the former represents labile oxygen functionalities (e.g., lactone and carboxylic functionalities) and the latter represents strongly bonded oxygen atoms (e.g., ether and ketonic functionalities). The A(S) and U(S) surface pseudo-species respectively describe active and non-reactive inorganic matter. Inorganic matter is represented by a pseudo-element ASH with molecular weight 62, representative of the average molecular weight of inorganic matter.[32]

As mentioned above, the same five surface functionalities are also introduced to describe the bulk region, and they are respectively labeled H(B), C_2O_2(B), CO(B), A(B), and U(B). An additional bulk pseudo-species labeled IB(B) is introduced to describe ashes that cannot be exposed to the reactive environment due to physical phenomena. Three bulk species are introduced to describe the carbonaceous structure: young carbon C_y(B), mature carbon C_m(B), and graphitic carbon C_g(B). These species aim to represent the increase in aromaticity and cluster size of the carbonaceous structure at

Table 1. Initial Species Introduced to Describe the Surface and Bulk Regions, the Functionality Described, Their Elemental Composition, the Number of Surface Sites Occupied by Each Surface Species N^{si}, and Their Molecular Weight MW

	species		elements					
functionality	surface	bulk	C	H	O	ASH	N^{si}	MW
hydrogen	H(S)	H(B)	0	1	0	0	1	1
carbonyl	CO(S)	CO(B)	1	0	1	0	1	28
carboxyl	C_2O_2(S)	C_2O_2(B)	2	0	2	0	2	56
young carbon	–	C_y(B)	1	0	0	0	1	12
mature carbon	–	C_m(B)	1	0	0	0	1	12
graphitic carbon	–	C_g(B)	1	0	0	0	1	12
active ashes	A(S)	A(B)	0	0	0	1	1	62
unreactive ashes	U(S)	U(B)	0	0	0	1	1	62
non-exposable ashes	–	IB(B)	0	0	0	1	0	62

increasingly severe pyrolysis conditions. The definition of these carbonaceous species is similar to that proposed by Maffei,[33] and it is in line with experimental observations by Keiluweit et al.[34] No initial pure carbonaceous surface species are introduced as the oxidation of the aromatic layer starts from functionalities on the edges (i.e., H(S), C_2O_2(S), CO(S), A(S), and U(S)). Nevertheless, bulk carbon is exposed during the oxidation process, forming the surface species C_y(S), C_m(S), and C_g(S).

2.2. Quantitative Characterization of Initial Species.

To describe the initial particle, a constrained minimization procedure is performed. The minimization aims to recover the surface and bulk species' distribution. Each species i in region P is characterized by a molar and mass fraction, respectively labeled x_P^i and y_P^i. For surface species, a distinction is made between the site and species molar fractions, respectively labeled $x_{s,si}$ and $x_{s,sp}$. The distribution depends on the relative amounts of bulk and surface regions, which are quantitatively estimated through the mass-specific surface S_g, the density of surface sites Γ, and the skeletal (i.e., true) density ρ_{sk}.

The characterization procedure requires as input values ("inp") the particle dry mass elemental composition $\omega_e^{p,inp}$ and the particle initial porosity ϵ_0. The mass specific surface S_g^{inp} and the density of surface sites Γ^{inp} are evaluated with the following empirical correlations:

$$S_g^{inp} = \frac{a_s}{c_s}\frac{1}{\left(\frac{H}{C}\right)_{wt}}\, e^{-(\ln(H/C)_{wt} - b_s)^2/2c_s^2} \tag{1}$$

$$\Gamma^{inp} = \left(1 + a_\Gamma\left(\frac{H}{C}\right)_{wt}\right)(b_\Gamma\, e^{-c_\Gamma \omega_C^{inp,daf}} + d_\Gamma) \tag{2}$$

$$\rho_{sk} = a_\rho\, e^{b_\rho (H/C)_{wt}} + c_\rho \tag{3}$$

Further information on the correlation development and their parameters is discussed in depth in paragraphs S-II.I.I, S-II.I.II, and S-II.I.III of the Supporting Information. A sensitivity analysis to the correlations is also reported in section S-IV of the Supporting Information.

The skeletal density does not affect the characterization but impacts the oxidation. The described correlations are not employed if information on Γ^{inp}, S_g^{inp}, or ρ_{sk} is available. Only chars that have developed their oxygen-accessible pore network are considered, and a threshold value $S_g^{inp} > 100$ m^2 g^{-1} is chosen, as discussed in paragraph S-II.I.II of the Supporting Information.

The objective function f is constructed and minimized as

$$\begin{cases} \min\limits_{x_{s,sp}, x_b, \Gamma, S_g}\left(f = (1 - x_b^{Ct(B)})^2 + w_S\left(\frac{S_g - S_g^{inp}}{S_g^{inp}}\right)^2 + w_\Gamma\left(\frac{\Gamma - \Gamma^{inp}}{\Gamma^{inp}}\right)^2\right) \\ \text{s.t. } \omega_e^p = \omega_e^{p,inp} \qquad e = C, H, O, ASH \\ \text{s.t. } x_b^{i(B)} = x_{s,sp}^{i(S)}(1 - x_b^{Ct(B)} - x_b^{IB(B)}) \qquad i \neq Ct, IB \\ \text{s.t. } \frac{\omega_A^p}{\omega_U^p} = \frac{\theta}{1-\theta} \\ \text{s.t. } \omega_{IB(B)}^p = \max(0, \omega_{ASH}(1 - MW_{ASH}\Gamma S_g\sqrt{1 - \psi \ln \omega_{ASH}})) \\ \text{s.t. } \frac{m_b}{m_p} > 0.5 \end{cases} \tag{4}$$

where ω^p is the mass fraction with respect to the total char particle, e refers to the element, i and l refer to the species, m_b is the mass of the bulk region, m_p is the total particle mass, MW_i is the molecular weight of species i, θ is the active fraction of inorganic matter, ψ is the Random Pore Model (RPM)[35,36] structural parameter, and w is the weight of the minimization function. The values without the script "inp" are the values employed in the oxidation model. An in-depth description of the minimization procedure is reported in section S-II of the Supporting Information. The particle is assumed chemically homogeneous. For this reason, the relative amounts of all species present both in bulk and in the surface region are equal in the two regions. The minimization function does not distinguish among the different carbonaceous species nor between the oxygenated species. For this reason, eq 4 exhibits Ct(B), which is the sum of the three carbonaceous species, and Ot(B), which is the sum of the oxygenated species. The relative amounts of the carbonaceous and oxygenated species are post-processed through a parameter $\beta \in [0; 1]$,

$$\beta = 0.5121\left[1 + \tanh\left(14.91\frac{\omega_C^{inp}}{1 - \omega_{ASH}^{inp}} - 13.05\right)\right] \tag{5}$$

This parameter aims to evaluate the aromaticity, age, and size of aromatic clusters present in the char particle through the particle elemental composition.[37−39]

All inorganic-bound elements are considered in ω_{ASH}^{inp}. The amounts of ashes that can be exposed correspond to the amounts the final particle is able to accommodate in the surface region. In turn, the particle mass fraction of IB(B), $\omega_{IB(B)}^p$, is evaluated as the mass of ashes that cannot be accommodated. As discussed in sections 3.4 and 3.5, considering a constant surface site density and employing the RPM, the final surface region mass can be evaluated a priori. The surface evolution requires evaluation of the structural parameter ψ. This parameter is evaluated from the initial particle porosity[40] as

$$\psi = -\frac{1}{\ln(1 - \epsilon_0)}\zeta \tag{6}$$

where ζ is the deviation of the ψ parameter for the considered pore size distribution with respect to a uniform distribution. A value $\zeta = 5$ is employed to describe all char particles. The considered value represents a log-normal pore size distribution with similar amounts of pores of both mean size and one-tenth of the mean size. As evaluated through a sensitivity analysis (section S-IV of the Supporting Information), ζ has a mild influence on the oxidation behavior.

The ashes that can be exposed are lumped into active (A) and unreactive (U) species. Their relative amounts are evaluated through the active fraction of inorganic matter θ, which is in turn estimated with information on the inorganic composition. All inorganic complexes are classified in three families: *ha*, complexes which exhibit the highest reactivity (e.g., K and Na); *ma*, complexes which exhibit moderate reactivities (e.g., Ca and Fe); *la*, all inorganic elements that exhibit low reactivity. Considering studies of Pflieger et al.,[41] it is assumed the *ma* family has one-fourth the reactivity of the *ha* family. If no information on the specific particle is available, the ashes composition of the virgin biomass is employed. In this case, however, the *ma* family is assumed to have a higher catalytic activity to represent its lower volatilization tendency.[42] To summarize, θ is evaluated

$$\begin{cases} \theta = \dfrac{\omega_{ha}^{\mathrm{ASH}} + 0.25\omega_{ma}^{\mathrm{ASH}}}{\omega_{ha}^{\mathrm{ASH}} + \omega_{ma}^{\mathrm{ASH}} + \omega_{la}^{\mathrm{ASH}}} & \text{if char composition} \\ \theta = \dfrac{\omega_{ha}^{\mathrm{ASH}} + 0.5\omega_{ma}^{\mathrm{ASH}}}{\omega_{ha}^{\mathrm{ASH}} + \omega_{ma}^{\mathrm{ASH}} + \omega_{la}^{\mathrm{ASH}}} & \text{if virgin biomass composition} \end{cases} \tag{7}$$

where ω_i^{ASH} is the mass fraction of family i in the total ashes. For instance, $\omega_{ha}^{\mathrm{ASH}}$ is the total mass fraction of K and Na oxides in the total inorganic matter.

3. GOVERNING EQUATIONS

Modeling the reacting particle requires a set of equations for each phase/region. Table 2 summarizes the differential equations used in the present model in terms of phase, type, state variables, number, and the specific section in which they are discussed. The solution of the system of $N_g + N_b + N_s + 3$ differential equations is employed to model the evolution of the particle. The energy balance equation is not considered as thermal equilibrium is assumed at each time-step.

Table 2. Differential Equations Introduced for Each Phase/Region, Their Numbers, and the Paragraphs in Which They Are Discussed

phase	equation	variable	no. eqs[a]	section
gas	species conservation - mass fractions	y_g^i	N_g	3.2
	total mass conservation	m_g	1	
solid bulk	species conservation - mass	m_i^b	N_b	3.3
solid surface	species conservation - molar site fractions	$x_{s,si}^i$	N_s	3.4, 3.5
	surface evolution	A	1	
	active site density conservation	Γ	1	

[a] The total number of differential equations is $N_g + N_b + N_s + 3$.

An initial particle volume of 1 mm^3 is considered for all char samples. During the oxidation process, the particle volume is assumed constant assuming the inorganic structure allows to retain the particle structure. The variation in solid volume is evaluated through the total particle mass, as it accounts for both the mass of bulk and surface regions, and it is used to evaluate the void fraction. The skeletal density ρ_{sk} is also assumed constant throughout the oxidation process. Before addressing the particle evolution and the coupling of the physical and chemical description (section 3.5), it is required to discuss the formulation of the reaction mechanism. A brief account on the numerical methodology is given in section 3.6.

3.1. Introduction to the Heterogeneous Reaction Mechanism.

The solid-phase mechanism is coupled with a detailed homogeneous gas-phase mechanism,[43−47] in order to account for both solid-phase reactions and secondary gas-phase reactivity. The solid-phase mechanism is composed of 205 non-reversible reactions employing a CHEMKIN-like[48] formulation, and it is attached as Supporting Information in the file "kinetic.surface". Table 3 reports the reaction classes introduced in the solid-phase mechanism. Decomposition reactions describe the desorption steps, and are the only reactions that may involve both bulk and surface species. Decomposition reactions that convert a bulk species in the corresponding surface species are referred to as bulk exposure reactions. In addition to bulk exposure reactions, bulk species also undergo volumetric isomerization reactions.

Table 3. Reaction Classes Introduced in the Present Solid-Phase Mechanism for Gas (G), Surface (X(S)), and Bulk Species (W(B))

reaction class	formulation	reactants
surface adsorption	$X_1(S) + G \rightarrow X_2(S)$	gas and surface species
surface isomerization	$X_1(S) \rightarrow X_2(S)$	surface species
surface decomposition	$W(B) + X_1(S) + G_1 \rightarrow X_2(S) + G_2$	gas, surface, and bulk species
volumetric isomerization	$W_1(B) \rightarrow W_2(B)$	bulk species

The rate of a surface reaction r_j^s in Table 3 is expressed as

$$\begin{cases} r_j^s = k_j \displaystyle\prod_{i=1}^{N_j^R} C_{i,P}^{\eta_{i,j}} & \left[\dfrac{\mathrm{kmol}}{\mathrm{m}^2\,\mathrm{s}}\right] \\ C_{i,g} = x_g^i C_{tot}^g & \left[\dfrac{\mathrm{kmol}}{\mathrm{m}^3}\right] \\ C_{i,s} = x_{s,sp}^i \Gamma & \left[\dfrac{\mathrm{kmol}}{\mathrm{m}^2}\right] \\ C_{i,b} = a_i^{ex} & [-] \end{cases} \tag{8}$$

where k_j is the modified Arrhenius kinetic constant of reaction j, N_j^R the number of reactants involved in reaction j, $C_{i,P}$ the concentration of species i in phase P, x_g^i the gas molar fraction of species i, C_{tot}^g the total gas concentration, and a_i^{ex} the activity of the bulk species i in the mixture of bulk species that can be exposed (i.e., bulk species with a surface counterpart). Reaction orders $\eta_{i,j}$ of surface and gas species i involved in surface reaction j coincide with the stoichiometric coefficients. On the other hand, bulk species involved in surface reactions are of first order in their activities. For each reaction j, δ_j is defined as the variation of the number of surface sites due to reaction j. The presence of bulk species in surface reactions describes the regeneration and consumption of surface sites across the reaction. The bulk region is assumed to behave ideally, and the mixture activities coincide with the mixture bulk molar fractions.[49] Conceptual issues in the definition of activities arise as complete consumption of exposable bulk phase occurs ($m_{\mathrm{b}}^{\mathrm{ex}}/m_{\mathrm{b}}^{\mathrm{ex},0} < 10^{-7}$). In these conditions, bulk activities are assumed null for all bulk species to represent site regeneration cannot take place. Volumetric isomerisations are employed to describe graphitization (section 4.2) and ash deactivation (section 4.3). The reaction rate r_j^{v} of volumetric reaction j is evaluated as

$$\begin{cases} r_j^{\nu} = k_j \prod_{i=1}^{N_j^{\mathrm{R}}} C_{i,\mathrm{b}}^{\eta_{i,j}} & \left[\frac{\mathrm{kmol}}{\mathrm{m^3\,s}}\right] \\ C_{i,\mathrm{b}} = x_{\mathrm{b}}^{i} \frac{\rho_{\mathrm{sk}}}{\mathrm{MW}_i} & \left[\frac{\mathrm{kmol}}{\mathrm{m^3}}\right] \\ r_j^{\mathrm{s}\nu} = r_j^{\nu} \frac{1-\epsilon}{S} & \left[\frac{\mathrm{kmol}}{\mathrm{m^2\,s}}\right] \end{cases} \tag{9}$$

where MW_i is the molecular weight of species i. The order of reactions $\eta_{i,j}$ coincides with the stoichiometric coefficients $\nu_{i,j}$. Volumetric reactions r_j^{ν} are translated to a surface description $r_j^{\mathrm{s}\nu}$ through the porosity and volumetric specific surface area to simplify the mathematical notation in the following equations.

3.2. Mass Balance of the Gas Phase. An equation for the mass fraction y_{g}^{i} of each gas-phase species i and one for the total mass of gas m_{g} are introduced:

$$\frac{\mathrm{d}y_{\mathrm{g}}^{i}}{\mathrm{d}t} = \frac{\dot{m}_{\mathrm{diff}}^{i} + \dot{m}_{\mathrm{in}}^{i} - \dot{m}_{\mathrm{out}}^{i}}{m_{\mathrm{g}}} + \frac{R_{\nu}^{i} V_{\mathrm{g}} + R_{\mathrm{s}\to\mathrm{g}}^{i} A_{\mathrm{p}}}{m_{\mathrm{g}}} \mathrm{MW}_i - \frac{y_{\mathrm{g}}^{i}}{m_{\mathrm{g}}} \frac{\mathrm{d}m_{\mathrm{g}}}{\mathrm{d}t} \tag{10}$$

$$\frac{\mathrm{d}m_{\mathrm{g}}}{\mathrm{d}t} = \sum_{i=1}^{N_{\mathrm{g}}} \dot{m}_{\mathrm{diff}}^{i} + \dot{m}_{\mathrm{in}} - \dot{m}_{\mathrm{out}} + \sum_{i=1}^{N_{\mathrm{g}}} R_{\mathrm{s}\to\mathrm{g}}^{i} A_{\mathrm{p}} \mathrm{MW}_i \tag{11}$$

where $\dot{m}_{\mathrm{diff}}^{i}$ is the mass flow rate of species i due to diffusive fluxes (J), and $\dot{m}_{\mathrm{in}}^{i}$ and $\dot{m}_{\mathrm{out}}^{i}$ are the convective inlet and outlet mass flow rates of species i due to Darcy fluxes (D_{f}). Further information on the evaluation of mass flow rates is reported in section S-I in the Supporting Information. R_i is the formation rate of species i which is composed of two contributions: the volumetric formation rate R_{ν}^{i} due to homogeneous gas-phase reactions, and the surface formation rate $R_{\mathrm{s}\to\mathrm{g}}$ due to solid-phase reactions.

3.3. Mass Balance of the Solid Bulk. An equation for the mass m_{b}^{i} of each bulk species i is introduced:

$$\frac{\mathrm{d}m_{\mathrm{b}}^{i}}{\mathrm{d}t} = R_{\mathrm{b}}^{i} A_{\mathrm{p}} \mathrm{MW}_i \tag{12}$$

where volumetric bulk reactions are included in the formation rate R_{b}^{i} through eq 9.

3.4. Material Balance at the Solid Surface. At the solid surface one equation for the site fraction $x_{s,si}^{i}$ of each surface species i, one equation for the total particle surface A_{p}, and one equation for the density of surface sites Γ are introduced:

$$\frac{\mathrm{d}x_{\mathrm{s,si}}^{i}}{\mathrm{d}t} = \frac{N_i^{\mathrm{si}} R_{\mathrm{s}}^{i,\mathrm{sp}}}{\Gamma} - \frac{x_{\mathrm{s,si}}^{i}}{A_{\mathrm{p}}} \frac{\mathrm{d}A_{\mathrm{p}}}{\mathrm{d}t} - \frac{x_{\mathrm{s,si}}^{i}}{\Gamma} \frac{\mathrm{d}\Gamma}{\mathrm{d}t} \tag{13}$$

$$\frac{\mathrm{d}A_{\mathrm{p}}}{\mathrm{d}t} = -V_{\mathrm{p}} S_0 \left[\frac{\psi(1-\chi)}{2S_n} - \frac{S_n}{1-\chi}\right] \left(\sum_{i=1}^{N_{\mathrm{s}}} \Omega_{\mathrm{s}}^{i} + \sum_{i=1}^{N_{\mathrm{b}}} \Omega_{\mathrm{b}}^{i}\right) \frac{A_{\mathrm{p}}}{m_{\mathrm{p}}^{0}} \tag{14}$$

$$\frac{\mathrm{d}\Gamma}{\mathrm{d}t} = \sum_{j=1}^{N_{\mathrm{s}}^{r}} \delta_j r_j^{\mathrm{s}} - \frac{\Gamma}{A_{\mathrm{p}}} \frac{\mathrm{d}A_{\mathrm{p}}}{\mathrm{d}t} \tag{15}$$

where $R_{\mathrm{s}}^{i,\mathrm{sp}}$ is the rate of formation of species i, Ω^{i} is the mass rate of formation of species i, and N_s^{r} is the total number of solid-phase reactions r_j^{s}. The total surface evolution is described through the RPM[36] with respect to the initial volumetric specific surface area S_0 and the total particle volume V_{p}. The evolution of the normalized volumetric specific surface S_{n} is due to the structural parameter ψ and the variation of the particle mass conversion χ.

3.5. Consistency of Physical and Chemical Description. To the authors' knowledge, there is no model in literature describing the evolution of the density of surface sites. Therefore, the value estimated in the characterization (section 2.2) is assumed constant throughout the conversion process.[50] However, introducing independent assumptions on $\frac{\mathrm{d}\Gamma}{\mathrm{d}t}$, $\frac{dA_p}{dt}$ and $\sum_{j=1}^{N_{\mathrm{s}}^{\mathrm{r}}} \delta_j r_j^{\mathrm{s}}$ makes eq 15 overly constrained. Other works[26,28,29] address this issue introducing a free-site species. The fraction of sites occupied by this species is obtained not from eq 13 but from the closure of the site fractions, $\sum_{i=1}^{N_{\mathrm{s}}} x_{\mathrm{s,si}}^{i} = 1$. In the present work, we propose to address this issue implicitly in reaction mechanism dynamics which must be coupled to $\mathrm{d}(\Gamma A_{\mathrm{p}})$. This feature is achieved through surface decomposition reactions which are expressed by N_{b} "bulk exposure reactions" as

$$2W(\mathrm{B}) + X(\mathrm{S}) \to 2W(\mathrm{S}) + X \qquad \forall\ \mathrm{W(B)} \neq \mathrm{IB(B)} \tag{16}$$

$$X(\mathrm{S}) \to X \tag{17}$$

These reactions represent the same chemical phenomenon, but reaction 16 is composed of $N_{\mathrm{b}} - 1$ reaction-regenerating surface sites and results in a net increase of the number of surface sites ($\delta = 1$). On the other hand, reaction 17 consumes surface sites, resulting in a net reduction in the number of surface sites ($\delta = -1$). Although the stoichiometric coefficient of bulk species in reaction 16 is 2, exposure reactions kinetics remain first order in the activity of the bulk species involved (section 3.1). The kinetic constants slightly differ according to the bulk species involved as described in section 4.1.

Overall, the solid-phase reaction mechanism can be divided in three sets of reactions:

- r^{ne}: reactions not involving bulk species exposure as adsorption and isomerization (r46−r63, r145−r156, and r202−r205);
- r^{re}: bulk exposure reactions regenerating surface sites (r11−r18, r20−r27, r29−r36, r38−r45, r65−r72, r74−r81, r83−r90, r92−r99, r101−r108, r110−r117, r119−r126, r128−r135, r137−r144, r158−r165, r167−r174, r176−r183, r185−r192, and r194−r201);
- r^{co}: bulk exposure reactions consuming surface sites (r10, r19, r28, r37, r64, r73, r82, r91, r100, r109, r118, r127, r136, r157, r166, r175, r184, and r193).

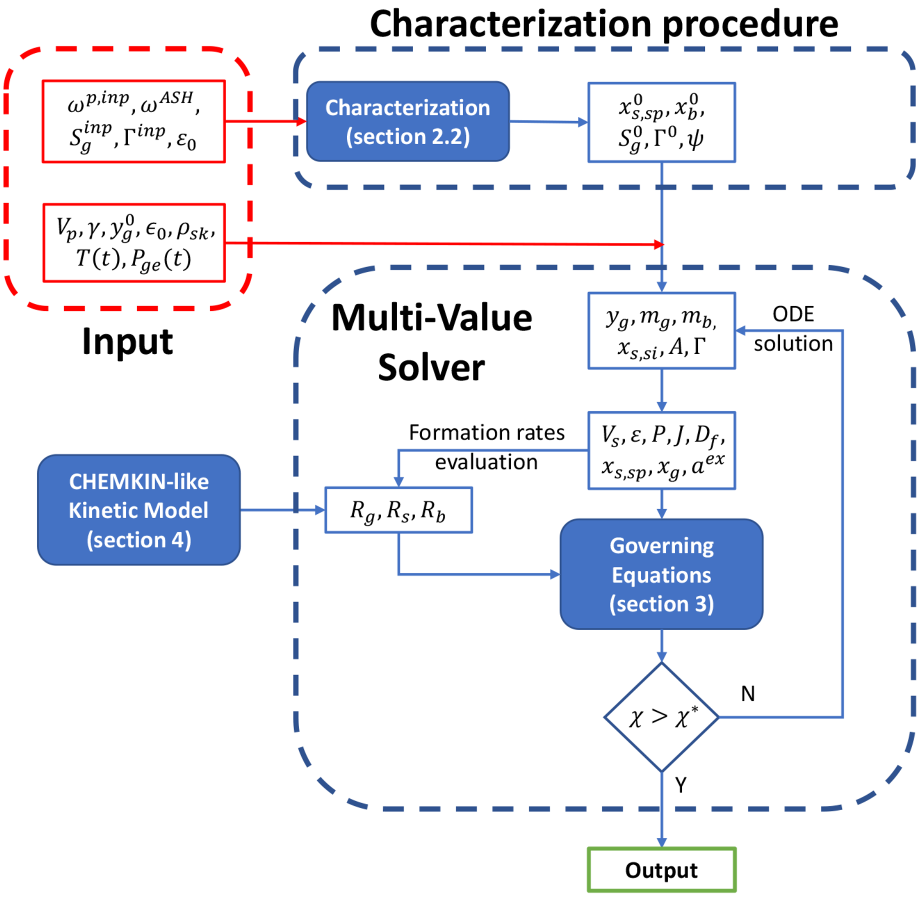

Figure 2. Schematic representation of the sub-models and variables employed in the developed software

Each set k is composed of several reactions j with reaction rates $r_j^{s,k}$ expressed as eq 8. In order to couple the kinetic mechanism with the surface moles evolution, r^{ne} and r^{co} are modulated through a consistency parameter α such that

$$R_s^{as,tot} = \sum_{j=1}^{N_s^{r,ne}} \delta_j r_j^{s,ne} + (1-\alpha)\sum_{j=1}^{N_s^{r,re}} \delta_j r_j^{s,re} + \alpha \sum_{j=1}^{N_s^{r,co}} \delta_j r_j^{s,co} \tag{18}$$

where $R_s^{as,tot}$ is the total molar site formation rate, the superscripts ne, re, and co refer to the set to which each reaction belongs, and $N_s^{r,k}$ is the number of reactions in set k. α acts as degree of freedom of eq 15 and is evaluated imposing the constraint on Γ. For simplicity, the surface site formation rate due to set k (R_s^k) and the total particle mass formation rate due to set k (Ω_t^k) are introduced:

$$R_s^k = \sum_{j=1}^{N_s^{r,k}} \delta_j r_j^{s,k} \qquad k = \text{ne}, \ \text{re}, \ \text{co} \tag{19}$$

$$\Omega_t^k = \sum_{i=1}^{N_s} \mathrm{MW}_i R_i^{s,k} + \sum_{i=1}^{N_b} \mathrm{MW}_i R_i^{b,k} \qquad k = \text{ne}, \ \text{re}, \ \text{co} \tag{20}$$

where $R_i^{P,k}$ is the formation rate of species i in phase P due to reactions of set k. Combining eq 15 with eqs 18, 19, and 20 and introducing the constraint on Γ, the following algebraic equation is obtained:

$$\begin{cases} 0 = R_s^{ne} + (1-\alpha)R_s^{re} + \alpha R_s^{co} - \dfrac{\Gamma}{A_p}\dfrac{dA_p}{dt} \\ \dfrac{dA_p}{dt} = \dfrac{dA_p}{d\chi}[\Omega_t^{ne} + (1-\alpha)\Omega_t^{re} + \alpha\Omega_t^{co}]\dfrac{A_p}{m_p^0} \end{cases} \tag{21}$$

where the dependence of conversion on the reaction mechanism is made explicit, and $\frac{dA_p}{d\chi}$ is the surface evolution with respect to conversion predicted by the RPM (eq 14). Equation 21 can be analytically rearranged to evaluate α:

$$\begin{cases} \alpha = \dfrac{R_s^{ne} + R_s^{re} + q(\Omega_t^{ne} + \Omega_t^{re})}{R_s^{re} - R_s^{co} + q(\Omega_t^{re} - \Omega_t^{co})} \\ q = \dfrac{\Gamma}{m_p^0}\dfrac{dA_p}{d\chi} \end{cases} \tag{22}$$

where q is introduced to simplify the mathematical notation. It is defined $\alpha \in [0, 1]$ since negative irreversible reaction rates do not have physical meaning. Therefore, if eq 22 yields a value outside the interval, α is constrained to the closest interval bound (i.e., 0 if $\alpha < 0$ or 1 if $\alpha > 1$). This occurs if R_s^{ne}, R_s^{re}, and R_s^{co} differ by several orders of magnitude. These differences are due to the formulation of the reaction mechanism, and the present formulation is not able to ensure a constant surface site density. Nevertheless, eq 15 allows Γ to vary without any inconsistency (i.e., $\sum_{i=1}^{N_s} x_{s,si}^i \neq 1$).

The present formulation fails as the bulk mass to be exposed, m_b^{ex}, approaches complete consumption. In these conditions bulk activities, and in turn r^{re}, are null, and eq 22 leads to a nonphysical increase in particle mass. In these conditions, it is chosen to extend the present formulation constraining α to the last value computed before complete exposable bulk consumption occurs. To avoid eq 15 being overly constrained, the constraint on surface evolution is removed, and it is simply evaluated to satisfy the constraint on Γ. It is chosen to modify eq 14 rather than eq 15, as the assumption on the surface site density is still appropriate. While the underlying structure is still mainly aromatic, the onset of additional physical phenomena may change the surface evolution mechanism (e.g., fragmentation). To summarize, surface evolution is evaluated as follows:

$$\begin{cases} \text{if } \dfrac{m_b^{ex}}{m_b^{ex,0}} > \lambda \rightarrow \dfrac{dA_p}{dt} = \left.\dfrac{dA_p}{dt}\right|_{RPM} \\ \text{if } \dfrac{m_b^{ex}}{m_b^{ex,0}} < \lambda \rightarrow \dfrac{dA_p}{dt} = \dfrac{A_p}{\Gamma}\displaystyle\sum_{j=1}^{N_s^r} \delta_j r_j^s \end{cases} \qquad (23)$$

where $\left.\frac{dA_p}{dt}\right|_{RPMPM}$ refers to the surface evolution predicted by the Random Pore Model (eq 14). The threshold value $\lambda \rightarrow 0$ is also employed in defining the exposable mixture activities (section 3.1).

3.6. Numerical Methodology. The numerical methodology employed in the present work is composed of two distinct tools: char characterization and char time-evolution. Figure 2 schematically represents the methodology involved. Char characterization is performed through an in-house MATLAB code. The minimization is performed employing the commercial "sqp" fmincon algorithm, while the "trust-region-dogleg" fsolve algorithm is employed to obtain the starting minimization value (section S-II in the Supporting Information).

To compute the particle time-evolution, a C++ in-house software was developed based on OpenSMOKE++.[51] The software employs the quantitative species distribution obtained through the characterization procedure, particle structural information, and the CHEMKIN-like kinetic mechanism. The time integration is performed with the OpenSMOKE++ MultiValueSolver employing the Gear method until 99.99% of the initial mass is consumed. The solution of the ODE system is coupled with the imposed temperature ($T(t)$) and gas environment pressure ($P_{ge}(t)$) to compute all additional variables.

4. SOLID-PHASE KINETIC MODEL

To the authors' knowledge, few theoretical studies on oxidation reactions of aromatic clusters are available in literature,[52−59] but, to properly quantify the lattice strain in solid-phase oxidation, large aromatic clusters must be considered as model compounds. However, the definition of model molecules proves conceptually challenging due to the intrinsic statistical description of the char structure. To develop a reaction mechanism consistent with the statistical structure, several authors introduced the distributions of activation energy method.[24−26,60,61] These studies are taken as reference to define the present reaction mechanism and its kinetic parameters. However, the statistical nature of the phenomenon is addressed through bulk exposure reactions. Several kinetic constants are obtained from the experimental study of Tilghman and Mitchell.[26] However, as additional reactions are introduced, several kinetic constants were determined considering the experimental behaviors of different chars since no suitable theoretical study was found. Nevertheless, theoretical evaluation of reaction pathways and kinetic parameters is expected to improve model predictions. The complete reaction mechanism is attached as Supporting Information in the file "kinetic.surface", and comprises of 17 pseudo-species and 205 reactions. The sensitivity analyses to the kinetic constants under different conditions of interest are reported in section S-IV of the Supporting Information.

4.1. Decomposition of Initial Surface Species. The species H(S) undergoes a lumped abstraction initiated by molecular oxygen to form gaseous water. This reaction aims to represent hydrogen removal by external agents exposing an underlying bulk species. As described in paragraph 3.5, each exposure reaction is written as $N_b - 1$ reactions regenerating surface sites (i.e., one for each bulk species to be exposed) and a single reaction consuming surface site. Each bulk species represents a different structure with different complex stability; therefore, the kinetic parameters of each reaction are slightly different. The difference in reactivity is assumed due to different activation energies, similarly to the distribution presented by Haynes and co-workers,[24,60] and Table 4 reports the kinetic parameters. These differences are developed considering the mass loss profiles of several carbonaceous materials, and all exposure reactions follow the same approach. Hydrogen removal exposing hydrogen or oxygen is assumed to exhibit the highest reactivity since heteroatoms represent non-aromaticity and defects and therefore affect lattice rigidity. With respect to heteroatoms, exposure of young carbon $C_y(B)$ exhibits a 2 kcal mol^{-1} higher activation energy, and graphitic carbon $C_g(B)$ has a 3 kcal mol^{-1} higher activation energy with respect to $C_y(B)$. Exposure of mature carbon $C_m(B)$ is assumed as the geometric average of young and graphitic carbon exposure, while removal of hydrogen to expose active and unreactive ashes is assumed equal to $C_g(B)$ exposure. Site consumption is assumed as the geometric average of the highest and lowest kinetic constant as it is reasonable to expect

Table 4. Hydrogen Removal by Gas-Phase O_2 Exposing Different Bulk Species and the Corresponding Modified Arrhenius Kinetic Parameters (Units cal, mol, cm, s)

	reaction	A	n	E_{act}
r1	$H(S) + O_2 \rightarrow 0.5H_2O + 0.75O_2$	5×10^{10}	0	27500
r2	$2C_y(B) + H(S) + O_2 \rightarrow 0.5H_2O + 0.75O_2 + 2C_y(S)$	5×10^{10}	0	27000
r3	$2C_m(B) + H(S) + O_2 \rightarrow 0.5H_2O + 0.75O_2 + 2C_m(S)$	5×10^{10}	0	28500
r4	$2C_g(B) + H(S) + O_2 \rightarrow 0.5H_2O + 0.75O_2 + 2C_g(S)$	5×10^{10}	0	30000
r5	$2H(B) + H(S) + O_2 \rightarrow 0.5H_2O + 0.75O_2 + 2H(S)$	5×10^{10}	0	25000
r6	$2CO(B) + H(S) + O_2 \rightarrow 0.5H_2O + 0.75O_2 + 2CO(S)$	5×10^{10}	0	25000
r7	$C_2O_2(B) + H(S) + O_2 \rightarrow 0.5H_2O + 0.75O_2 + C_2O_2(S)$	5×10^{10}	0	25000
r8	$2A(B) + H(S) + O_2 \rightarrow 0.5H_2O + 0.75O_2 + 2A(S)$	5×10^{10}	0	30000
r9	$2U(B) + H(S) + O_2 \rightarrow 0.5H_2O + 0.75O_2 + 2U(S)$	5×10^{10}	0	30000

it to be of similar orders of magnitude as other reactions (section 3.5).

$C_2O_2(S)$ decomposition follows two pathways: release of CO_2 with formation of surface carbon (r10−r18), or release of CO with formation of CO(S) (r19−r27). The first one describes the release of weakly bonded groups (e.g., decarboxylation reactions), while the second one refers to structural rearrangement forming more stable groups (e.g., decarbonylation reactions). The kinetic parameters of the first pathways are derived from Tilghman and Mitchell's reaction mechanism,[26] where the distribution of activation energies formulation is integrated[60] and fitted to an Arrhenius form in the temperature range $T = 500-1500$ K. The parameters of the second pathway are calibrated so that the global CO-to-CO_2 selectivity is in accordance with the literature[26,62−64] (section 4.4).

The decomposition of CO(S) also follows two pathways releasing either CO (r28−r36) or CO_2 (r37−r45). The decarbonylation kinetic constant is defined by analogy to gas-phase phenoxy radical decomposition.[65] It is assumed that phenoxy and ketonic/ether functionalities exhibit similar reactivities as the aromatic moiety induces a resonance stabilization. However, as the aromatic cluster also hinders intramolecular rearrangements due to its rigidity, a penalty to the activation energy of 10 kcal mol^{-1} is considered. Table 5 reports the kinetic parameters of the CO(S) and $C_2O_2(S)$ decomposition exposing graphitic carbon. The kinetic parameters for other reactions belonging to the same class are reported in the Supporting Information and are obtained analogously to those for hydrogen removal (Table 4).

Table 5. Decomposition of CO(S) and $C_2O_2(S)$ Exposing $C_g(B)$ and the Corresponding Modified Arrhenius Kinetic Parameters (Units cal, mol, cm, s)

	reaction	A	n	E_{act}
r13	$2C_g(B) + C_2O_2(S) \rightarrow 2C_g(S) + CO_2 + C_g(S)$	2×10^8	0	34000
r22	$2C_g(B) + C_2O_2(S) \rightarrow 2C_g(S) + CO + CO(S)$	4×10^{10}	0	44000
r31	$2C_g(B) + CO(S) \rightarrow 2C_g(S) + CO$	1×10^{14}	0	63000
r40	$2C_g(B) + CO(S) + O_2 \rightarrow 2C_g(S) + CO_2 + 0.5O_2$	4×10^{14}	1	53000

4.2. Carbon Reactions. Decomposition of the initial surface species exposes bulk carbon to the gaseous phase as a surface carbon representing both σ and π radicals. Three carbon species having different reactivities are introduced to represent the influence of the carbonaceous structure on the radical reactivity (e.g., resonance phenomena, lattice strain, cluster size). Three reaction pathways are introduced for each surface carbon. Although few modifications are introduced, these reactions are defined similarly to Tilghman and Mitchell's work,[26] considering lumped adsorption of oxygen and isomerization in a single dual-site adsorption step, forming oxygenated complexes. Since interactions of different carbons are accounted for, each pathway is represented by $N_{C(S)}!$ reactions, where $N_{C(S)}$ is the number of surface carbon introduced (i.e., 3). A key feature of this model is the approximation of these complexes to behave equally to the oxygen characterization species, allowing to represent them with the same lumped pseudo-species $C_2O_2(S)$ and CO(S), instead of increasing the overall number of species.

As described by Tilghman and Mitchell,[26] the first adsorption pathway represents associative oxygen adsorption to form the species $C_2O_2(S)$ (r46−r51), while the second pathway represents dissociative oxygen adsorption and forms two CO(S) species (r52−r57). As the CO(S) species has a significantly higher reactivity compared to the species proposed by Tilghman and Mitchell,[26] CO desorption is not lumped in the present reaction. The third reaction represents the single step high temperature CO release proposed by Tilghman and Mitchell[26] (r58−r63). Table 6 reports the kinetic parameters of the three pathways for graphitic and young carbon oxidations. For the first two pathways of adsorption on graphitic carbon $C_g(S)$ we adopt similar parameters as in Tilghman and Mitchell,[26] whereas the third pathway becomes dominant at ∼1300 K. For young carbon, the higher reactivity is due to a lower activation energy, while preserving the same selectivity to the three pathways. As with decomposition to expose bulk mature carbon, the kinetic constant of surface mature carbon oxidation is assumed as the geometric average of $C_g(S)$ and $C_y(S)$ oxidation constants. Similarly, the kinetic parameters of interactions between different carbons are taken as the geometric average of the non-interacting reactions. For instance, the activation energy of low-temperature adsorption on neighboring $C_g(S)$ and $C_y(S)$ is 26000 kcal mol^{-1}, i.e., average of r46 and r48.

Table 6. Dual-Site Graphitic and Young Carbon Oxidation Reactions and the Corresponding Modified Arrhenius Kinetic Parameters (Units cal, mol, cm, s)

	reaction	A	n	E_{act}
r46	$2C_g(S) + O_2 \rightarrow C_2O_2(S)$	5×10^{19}	0	29000
r48	$2C_y(S) + O_2 \rightarrow C_2O_2(S)$	5×10^{19}	0	23000
r52	$2C_g(S) + O_2 \rightarrow 2CO(S)$	1×10^{22}	0	40000
r54	$2C_y(S) + O_2 \rightarrow 2CO(S)$	1×10^{22}	0	34000
r58	$2C_g(S) + O_2 \rightarrow CO(S) + CO$	6×10^{23}	0	50000
r60	$2C_y(S) + O_2 \rightarrow CO(S) + CO$	6×10^{23}	0	44000

The described pathways introduce a single lumped reaction to represent oxygen dual site adsorption, where the lumped elementary steps consist of single site adsorptions followed by internal addition on a neighboring surface carbon C(S). However, oxygen single site adsorption may be followed also by internal addition on neighboring hydrogen or internal H-abstraction. These internal additions and H-abstractions are represented introducing a single lumped pathway of dual site adsorption on any neighboring C(S) and H(S) (r64−r90). This reaction forms gaseous water exposing any underlying bulk species, while the surface carbon is oxidized to form the complex $C_2O_2(S)$. No reaction to form CO(S) is introduced as internal additions and H-abstractions are low temperature pathways, but interactions of all surface carbons with H(S) are considered. The kinetic parameters are defined with respect to low temperature dual site oxygen adsorption. Both a lower activation energy and frequency factor are introduced as carbon oxidation is expected to have higher sensitivity to temperature. As with dual-site carbon oxidation, the reactivity of the different carbons is represented by different activation energies. The different reactions to expose different bulk species are defined similarly to hydrogen removal reactions reported in Table 4, while Table 7 reports the kinetic parameters of the reaction of $C_y(S)$ and $C_g(S)$ exposing $C_g(B)$. Complex-enhanced dual-site oxygen adsorption on

Table 7. Interactions of $C_y(S)$ and $C_g(S)$ with H(S) and CO(S) and Their Modified Arrhenius Kinetic Parameters (Units cal, mol, cm, s)

	reaction	A	n	E_{act}
r67	$2C_g(B) + C_g(S) + H(S) + O_2 \rightarrow 2C_g(S) + 0.5C_2O_2(S) + 0.5H_2O + 0.25O_2$	8×10^{18}	0	25000
r85	$2C_g(B) + C_y(S) + H(S) + O_2 \rightarrow 2C_g(S) + 0.5C_2O_2(S) + 0.5H_2O + 0.25O_2$	8×10^{18}	0	22000
r94	$2C_g(B) + CO(S) + C_g(S) + O_2 \rightarrow 2C_g(S) + CO(S) + CO + 0.5O_2$	5×10^{19}	0	31000
r112	$2C_g(B) + CO(S) + C_y(S) + O_2 \rightarrow 2C_g(S) + CO(S) + CO + 0.5O_2$	5×10^{19}	0	28000
r121	$2C_g(B) + CO(S) + C_g(S) + O_2 \rightarrow 2C_g(S) + CO(S) + CO_2$	3×10^{19}	0	27000
r139	$2C_g(B) + CO(S) + C_y(S) + O_2 \rightarrow 2C_g(S) + CO(S) + CO_2$	3×10^{19}	0	24000

CO(S) and any surface carbon C(S) is also considered similarly to Tilghman and Mitchell's work.[26] Two reaction pathways to release either CO (r91−r117) or CO_2 (r118−r144), both regenerating CO(S), are considered. Compared to Tilghman and Mitchell's work, the latter has a slightly different stoichiometry allowing to expose all bulk species. The reactions between CO(S) and $C_g(S)$ have the same reactivity as in Tilghman and Mitchell[26] at 800 K. Interactions with the other surface carbons are defined similarly to carbon−hydrogen interaction. Table 7 reports the kinetic parameters of adsorption on $C_y(S)$ and $C_g(S)$, exposing graphitic bulk carbon.

To describe the annealing process, carbon graphitization reactions for both bulk and surface carbon are also considered (r145−r150). The kinetic parameters of these reactions are adopted from Maffei's work[33] and are applied for both surface and bulk carbons.

4.3. Presence of Ashes. The presence of ashes simultaneously enhances and inhibits particle conversion.[66] Several studies[41,42,67−69] show that different inorganic complexes affect char conversion in different ways. In general, transition, alkaline earth, and alkali metals undertake redox reactions transferring the oxidizing or gasifying agent from gas to solid phase. The reduced alkali metals also interact with the aromatic layers aiding decomposition reactions.[70] On the other hand, inhibition effects arise as mineral matter occupies part of the particle volume and surface. This "dilution" effect is described through eq 8 (section 3.1) as surface fraction and bulk activities decrease due to the presence of ashes.

To account for the catalytic effects, several low-temperature reactions between all surface species and active ashes A(S) are considered. The species A(S) accounts for both the reduced and oxidized state, and all the introduced reactions lump adsorption and surface reactions in a single step. Two ash carbon oxidation pathways (r151−r156) account for formation of $C_2O_2(S)$ and CO(S). Interactions with all surface carbons are considered with the same selectivity as low temperature carbon dual site adsorptions (r46−r51, r52−r57). Ashes interact with other species enhancing oxidation and decomposition of H(S) (r157−r165), CO(S) (r166−r183), and $C_2O_2(S)$ (r184−r201). Both surface oxides decompose to CO and CO_2, but the selectivity toward CO is enhanced to account for the effect of alkali metals. The catalytic effect decreases progressively due to ash sintering and catalyst poisoning phenomena. These phenomena are accounted for with a single bimolecular high temperature reaction, forming unreactive ashes U(S) from active ashes A(S). Deactivation of A(S) with U(S) is also introduced.[42] Most deactivation phenomena can occur also in bulk phase, and therefore volumetric bimolecular bulk phase deactivation reactions are considered. Ash devolatilization is not considered in the present model. Table 8 reports the kinetic parameters of ashes reactions exposing graphitic carbons. Interactions with different surface carbons are defined in analogy to Table 7, while reactions exposing different bulk species are defined in analogy to Table 4.

Table 8. Ashes Reactions and Their Modified Arrhenius Kinetic Parameters (Units cal, mol, cm, s)

	reaction	A	n	E_{act}
r151	$A(S) + C_g(S) + O_2 \rightarrow A(S) + 0.5C_2O_2(S) + 0.5O_2$	1×10^{18}	0	15000
r154	$A(S) + C_g(S) + O_2 \rightarrow A(S) + CO(S) + 0.5O_2$	2×10^{20}	0	26000
r160	$2C_g(B) + A(S) + H(S) + O_2 \rightarrow 2C_g(S) + A(S) + 0.5H_2O + 0.75O_2$	1×10^{17}	0	14000
r169	$2C_g(B) + A(S) + CO(S) \rightarrow 2C_g(S) + A(S) + CO$	3×10^{15}	0	30000
r178	$2C_g(B) + A(S) + CO(S) + O_2 \rightarrow 2C_g(S) + A(S) + CO_2 + 0.5O_2$	4×10^{15}	1	20000
r187	$2C_g(B) + A(S) + C_2O_2(S) \rightarrow 2C_g(S) + A(S) + CO_2 + C(S)$	2×10^{14}	0	20000
r196	$2C_g(B) + A(S) + C_2O_2(S) \rightarrow 2C_g(S) + A(S) + CO + CO(S)$	7×10^{16}	0	30000
r202	$2A(S) \rightarrow 2U(S)$	5×10^{20}	0	55000
r203	$A(S) + U(S) \rightarrow 2U(S)$	5×10^{20}	0	55000
r204	$2A(B) \rightarrow 2U(B)$	7×10^{5}	0	55000
r205	$A(B) + U(B) \rightarrow 2U(B)$	7×10^{5}	0	55000

4.4. Oxidation Products. The only oxidation products of the present model are H_2O, CO, and CO_2. While pollutant formation is outside the scope of the present study, to the authors' knowledge no systematic study on water formation is present in literature. On the other hand, the ratio CO to CO_2 was extensively studied in literature.[62−64,71−76] The experimentally measured ratios however differ by orders of magnitude according to each study. One of the reason may be secondary gas-phase oxidation of CO, which becomes dominant at temperatures higher than 1000 K for residence times in the order of minutes. However, modeling the exact gas residence time requires detailed modeling of transport phenomena, which is outside the scope of the present work. The present model therefore proposes a temperature dependence of $\frac{R_{CO}}{R_{CO_2}}$ similar to the one proposed by Tilghman and Mitchell,[26] within the confidence bounds reported by Campbell.[28,61] The predicted temperature dependence is shown in Figure 3a in comparison with the models proposed by Tilghman and Mitchell,[26] Tognotti et al.,[62] and Arthur et al.[63] The present model predicts an apparent exponent for the partial pressure of oxygen at 800 K in agreement with other studies[62,72−74] as shown in Figure 3b. However, compared to the correlations, the model predicts different apparent exponent varying reaction temperatures. Particularly, the sensitivity of the CO to CO_2 ratio to oxygen increases at high temperatures due to single-site CO(S) decomposition being the dominant pathways (section S-IV of the Supporting Information).

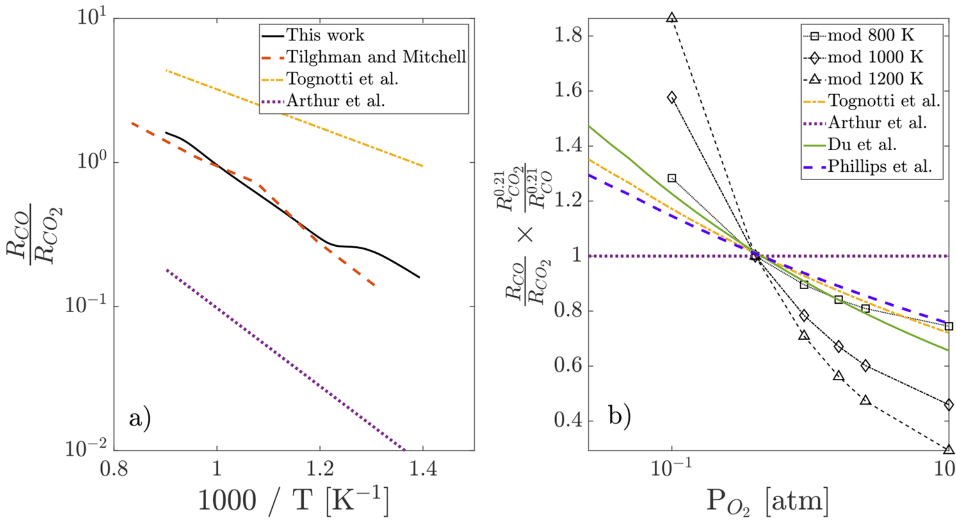

Figure 3. Comparison among the present work, Tilghman and Mitchell's model applied to Corn stover,[26] and correlations of Tognotti,[62] Arthur,[63] Du,[72] and Phillips[74] for (a) CO to CO_2 molar ratio function of the inverse of temperature T and (b) CO to CO_2 molar ratio at 800 K normalized to the value at 0.21 atm_{O_2} function of oxygen partial pressure

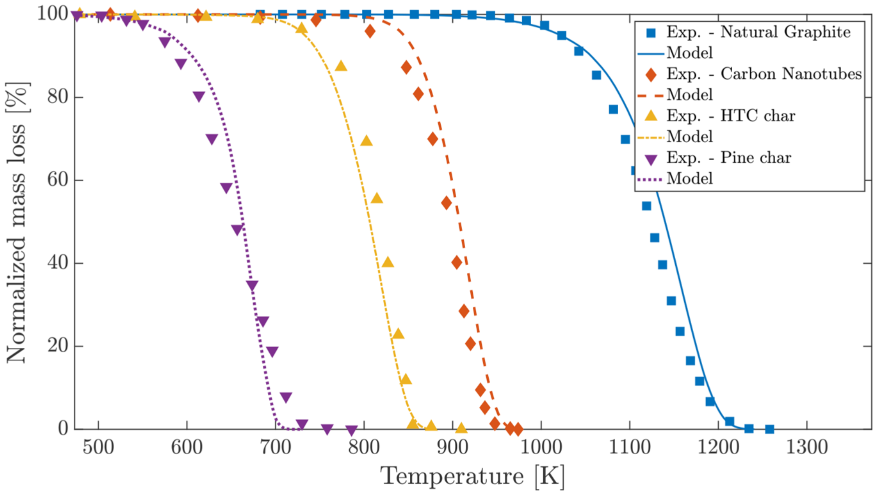

Figure 4. Mass loss of different carbonaceous materials in TGA-TPO. Comparison between experiments (marks) and model predictions (lines) for pine char at 5 K min^{-1} (Yu et al.[79]), hydrothermal cellulose char oxidized at 2 K min^{-1} (Dudder et al.[85]), carbon nanotubes oxidized at 20 K min^{-1} (Kim et al.[78]), and natural graphite oxidized at 10 K min^{-1} (Jiang et al.[77]).

Table 9. Model Validation Range in Terms of Particle Mass Percentages ω^p, Initial Specific Surface S_g^{inp} [$m^2\ g^{-1}$], Heating Rates HR [K min^{-1}], Isothermal Oxidation Temperature T_{iso} [K], and Pressure P [atm]

boundary	$\omega_C^{p,daf}$	$\omega_H^{p,daf}$	$\omega_O^{p,daf}$	$\omega_{ASH}^{p,dry}$	S_g^{inp}	HR	T_{iso}	$x_g^{O_2}$	P
lower	70	0	0	0	2	2	673	3.5×10^{-4}	1
upper	100	4	23	43	630	60	1173	5×10^{-1}	1

5. MODEL VALIDATION

The present model is validated in comparison with 93[13,14,41,64,77−87] different carbonaceous materials under different operating conditions. Very diverse oxidation behaviors are observed for different carbonaceous materials as observed in Figure 4. While the biochar sample exhibits an onset temperature at ∼550 K and reaches complete conversion at ∼700 K, the hydrothermal cellulose char and carbon nanotubes have their oxidation at temperatures ∼200 K higher. Lastly, natural graphite reactivity onset occurs at ∼1000 K, reaching complete conversion at ∼1200 K.

The model aims at reproducing the oxidation behavior of these different materials with a predictive approach, i.e., without any ad hoc tuning procedure. As reported in Table 9, the model was validated over a wide range of conditions. The considered chars are from different sources such as slow, flash, and ultra-flash pyrolysis processes. Similarly, different temperature and oxidizing environments were considered. However, the model would benefit from further investigations under elevated pressures. Only a selected set of validation targets is presented in the following section. The remaining validation comparisons are reported in Figure S4 in the Supporting Information.

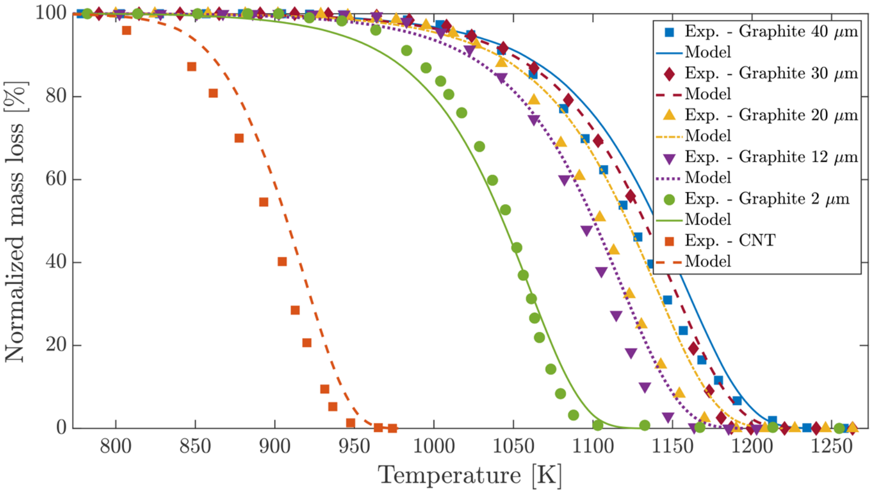

Figure 5. Mass loss in TGA-TPO of several natural graphite particles of different radius *r* (Jiang et al.[77]) and carbon nanotubes (Kim et al.[78]). Comparison between experimental results (marks) and model predictions (lines).

In order to achieve an enhanced degree of predictiveness, the model requires extensive data on both the chemical and physical structure. However, literature data are never complete, and therefore the missing particle data is inferred modeling the pyrolysis of the virgin biomass. Incomplete sets of data significantly affect the comparison between experimental observations and model predictions. Similarly, uncertainties in experimental measurements both of the particle structure and particle time-evolution do not allow straightforward comparisons. Nevertheless, the model captures the different reactivity of different particles in different operating conditions. While deviations between experiment and calculations are observed, the trends are described with reasonable accuracy over wide ranges of validation targets.

As described in section 2.2, the required input parameters are the dry particle elemental composition $\omega^{\mathrm{p,inp}}$, the ashes composition ω^{ASH}, the specific surface area $S_{\mathrm{g}}^{\mathrm{inp}}$, the surface site density Γ_{inp}, the porosity ϵ_0, and the skeletal density ρ_{sk}. Among the required information, porosity, ashes composition, and skeletal density exhibit milder effects on the present model. As literature data are seldom complete, the missing information of biochars is obtained modeling the pyrolysis of the virgin biomass. In the present work, the kinetic model proposed by Debiagi et al.[6] was employed to evaluate the dry and ash-free elemental composition. If the elemental or biochemical composition of the virgin biomass are not available, data on the average composition of the same family of biomasses is employed (the Phyllis database[88] may be used for this purpose). If not reported, the porosity of the biochar particle is evaluated adopting the anisotropic model proposed by Gentile et al.[89] If the initial porosity of the biomass is not available, data from the literature on similar biomasses are employed. The active and unreactive ashes are evaluated from both the total amounts of ashes of the particle and the composition of ashes. If the total ashes mass is not known, it is estimated from the initial biomass composition assuming no devolatilization occurs. The amounts of active ashes are evaluated from information either on the char particle, if available, or from average values on similar raw biomasses as described in section 2.2. If no information on skeletal density, surface site density, or specific surface of the char particle is reported, the correlations described in section 2.2 are employed. The correlations for the site and skeletal density were employed for all samples, as no study reported the corresponding information. Table S3 in the Supporting Information reports the complete set of input parameters for the simulations.

5.1. Carbon Oxidation.

Oxidation of carbonaceous materials allows to focus on the facets of carbon oxidation reactions. For this purpose, natural graphite and carbon nanotubes (CNT) are considered. Natural graphite was extensively studied, and information on porosity and skeletal density are also available.[90−92] Figure 5 shows the oxidation at 10 K min^{-1} of several natural graphite particles of different radii,[77] which are assumed to be composed of only bulk carbon and surface hydrogen. The different oxidation behaviors are due to the different ratio of edge and basal sites according to Jiang et al.[77] The present model recognizes the different reactivity due to the different experimental specific surface area, which indirectly relates to the ratio of basal to edge sites. The results allow to understand the influence of the specific surface area. Indeed, considering the 2 and 40 μm particles, an increase in S_{g} of 5 times corresponds to a difference in temperature offset of ∼100 K. The importance of the specific surface area is observed also considering experimental measurements on carbon nanotubes[78,93] shown in Figure 5, too. As for natural graphite, the specific surface is assumed to be occupied only by surface hydrogen. However, this hypothesis is not entirely appropriate, as the experimentally measured specific surface corresponds to both edge hydrogen and aromatic walls. Nevertheless, while aromatic carbon is assumed to react only as edge sites, Yao et al.[94] suggest that, for carbon nanotubes, oxidation of the bulk aromatic phase is concurrent to oxidation on the edges. The model correctly reproduces the different mass loss profiles of CNT compared to natural graphite. These differences are due to the higher specific surface, higher porosity, and higher heating rate (20 K min^{-1}). Even though the higher heating rate and porosity would shift the mass loss profile at higher temperatures, the 60 times higher specific surface yields a ∼150 K decrease in reaction temperature compared to the most reactive graphite particles.

5.2. Influence of the Operating Conditions.

Effects of operating conditions such as heating rate and oxygen

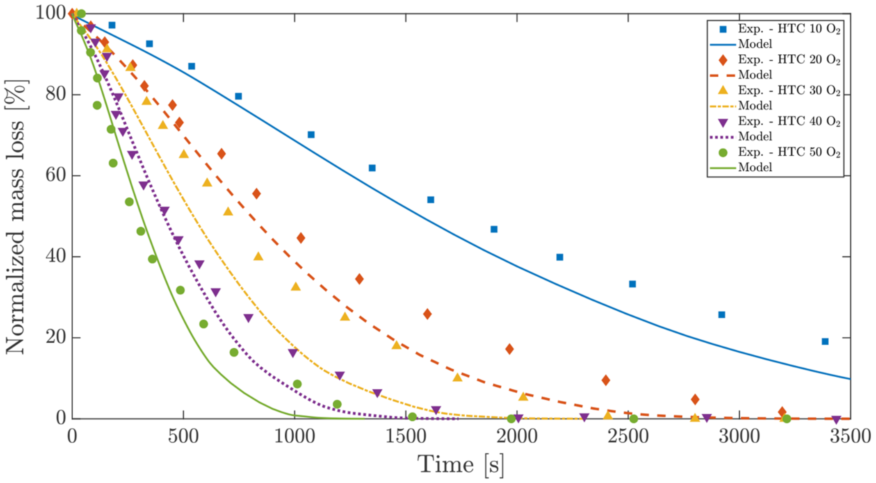

Figure 6. Mass loss in TGA-TPO of HTC char subjected to different oxygen concentrations (Pflieger et al.[41]). Comparison between experimental results (marks) and model predictions (lines).

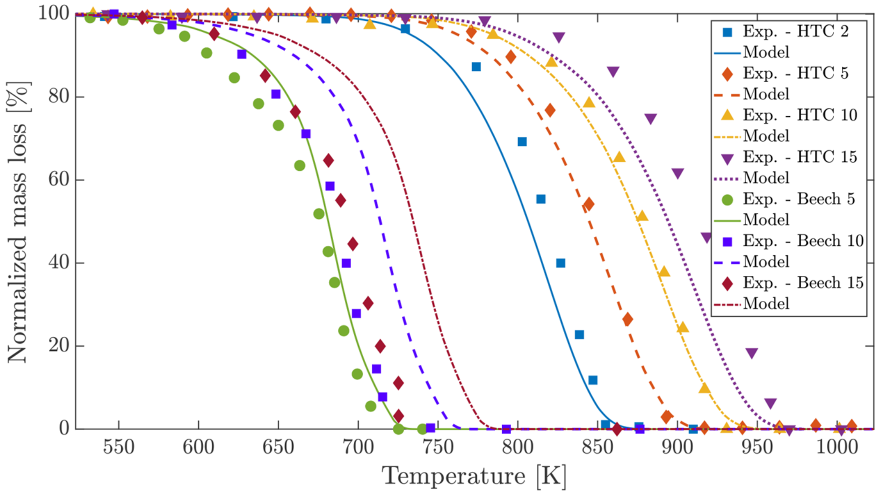

Figure 7. Mass loss in TGA-TPO of HTC char (Dudder et al.[85]) and Beech wood char (Branca and Di Blasi[87]) subjected to different heating rates. Comparison between experimental results (marks) and model predictions (lines).

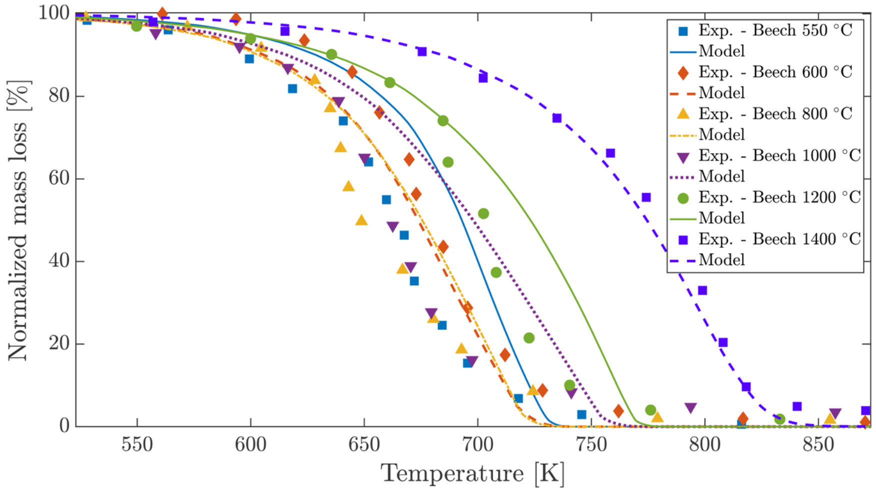

Figure 8. Mass loss in TGA-TPO for beech wood chars (Guizani et al.[13]) obtained at different pyrolysis temperatures (T). Comparison between experimental results (marks) and model predictions (lines).

concentration are captured by the model. Pflieger et al.[41] report measurements on isothermal oxidation of hydrothermal carbonized cellulose (HTC) char at 800 K under varying oxygen concentration. The sample hydrogen and oxygen

Table 10. Main Parameters of the Characterization Output for Beech Wood Chars:[13] **Surface Site Fractions ($x_{s,si}$ [%]), Bulk Mass Fraction of Species without an Initial Surface Counterpart (y_b [%]), Surface Site Density ($\Gamma \times 10^9$ [mol cm^{-2}]), Initial Mass-Specific Surface (S_g [m^2 g^{-1}]), and structural parameter (ψ)**

	$x_{s,si}$					y_b				
sample	H(S)	CO(S)	C_2O_2(S)	A(S)	U(S)	C(B)	IB(B)	Γ	S_g	ψ
550 °C	72.6	0.7	25.5	0.7	0.5	62.2	0.0	5.77	140	1.84
600 °C	71.2	2.9	23.6	1.4	0.9	72.8	0.0	4.37	283	1.53
800 °C	72.2	4.0	20.1	2.2	1.5	73.3	0.0	4.15	284	1.47
1000 °C	56.8	8.3	32.2	1.6	1.1	83.1	0.0	2.93	446	1.41
1200 °C	59.7	15.2	20.5	2.7	1.9	84.0	0.0	2.51	399	1.34
1400 °C	56.8	25.6	10.6	4.1	2.9	83.1	2.3	2.05	284	1.26

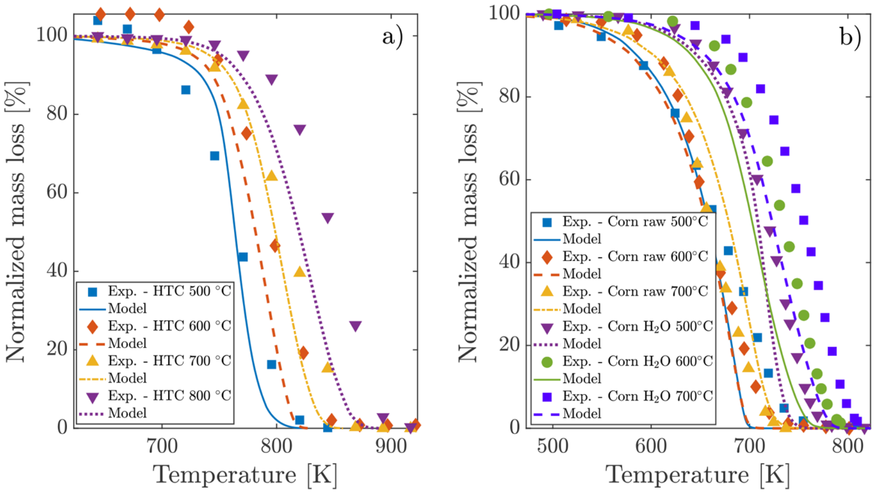

Figure 9. Mass loss in TGA-TPO for chars obtained at different pyrolysis temperatures from (a) HTC (Lotz et al.[98]) and (b) raw and H_2O leached corn stalk (Xu and Sheng[82]). Comparison between experimental results (marks) and model predictions (lines).

content are obtained from a linear interpolation between two analogous samples[14,85] employing the specific surface as the linearization variable. The initial porosity of the HTC sample is taken from Sheng et al.[95] The comparison between model predictions and experimental measurements is shown in Figure 6. The model describes the effect of oxygen concentrations due to carbon oxidation reactions and decomposition of CO(S). Since the experiments are performed at low temperatures, CO(S) decomposition with oxygen dominates over the pyrolytic pathway therefore concurring in increasing the model sensitivity to oxygen concentration. As observed from Figure 3 and discussed in section S-IV of the Supporting Information, at higher temperatures the model predicts a higher sensitivity to oxygen concentration as the high temperature rate determining step is dual-site carbon adsorption.

Figure 7 shows the model sensitivity to the heating rate compared to experimental measurements on HTC[85] and beech wood[87] char. HTC represents chars originated from severe biomass pyrolysis treatment, while the beech wood char represents chars resulted from mild pyrolysis conditions. The initial porosity of the chars were obtained from other studies.[95,96] For the beech wood char, the specific surface is estimated using the developed correlation (section 2.2), and the ash composition from studies on virgin beech wood.[32] For the high temperature pyrolysis chars, the model correctly describes the differences in reaction temperatures. On the other hand, for the low temperature chars the model exhibits a higher sensitivity to the heating rate compared to the experiments. This higher sensitivity is partly due to the lower activation energies of young carbon. Moreover, the dominant reaction pathways at low temperatures are complex-enhanced adsorptions and ashes interactions, characterized by lower activation energies.

5.3. Influence of the Pyrolysis Process.

Figure 8 shows the comparison of oxidation of biochars obtained from beech wood pyrolysis at different temperatures.[13] As the authors reported only the sample elemental composition, the specific surface was obtained from the developed correlation (section 2.2), while the initial porosity and ashes composition were obtained from other studies on beech wood.[32,96] The pyrolysis process affects the reactivity also in terms of characterization, and Table 10 reports the characterization output of the biochars shown in Figure 8. Consistently with the increase of carbon content from 75 to 90 wt%, the characterization predicts an increase in carbon bulk fraction as pyrolysis temperature increases. Similarly, the predicted decrease in surface hydrogen is consistent with the higher decrease in hydrogen content (from 3.6 to 0.9 wt%) with respect to the decrease in oxygen content (from 21 to 9 wt%). The increase in CO(S) site fraction is related also to the higher amounts of graphitic carbon. Indeed, while the 550 °C sample is composed of only young carbon, the 1200 °C sample is composed mainly of mature carbon, and the 1400 °C is composed of an equal mixture of mature and bulk carbon. The variation in ashes site fraction is consistent with the non-monotonic increase in ash content experimentally observed. On the other hand, the relative amounts of A(S) and U(S) are the same for all the

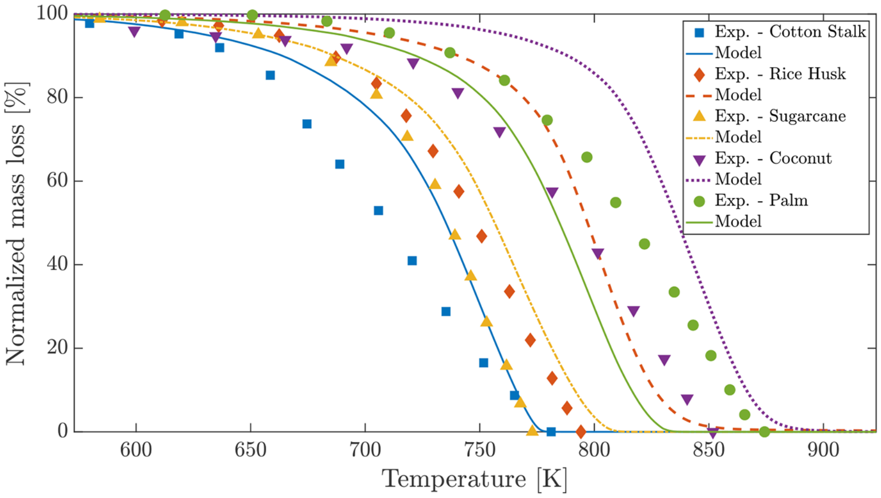

Figure 10. Mass loss in TGA-TPO for chars obtained from the same pyrolysis treatment applied to different biomasses (Windeatt et al.[80]). Comparison between experimental results (marks) and model predictions (lines).

samples since the same information on the virgin biomass was employed. The bulk fraction of IB(B) is not null only for the 1400 °C sample as the final number of surface sites (ΓS_g) is able to accommodate, and therefore expose, all ashes. While the surface site density and structural parameter decrease monotonically, the specific surface has a maximum corresponding to the 1000 °C sample. The characterization leads to similar outputs for the 600 and 800 °C samples since their elemental analysis is extremely similar.

The model is able to reasonably reproduce the different chars conversion rates, although it underestimates the conversion rate of the char sample produced at 1000 °C. The predicted lower reactivity is due to the lower amounts of ashes with respect to both the 800 and 1200 °C samples. On the other hand, the model predicts a maximum reactivity for the 800 °C sample in line with experimental measurements. Contrary to experimental results, the 550 °C sample is predicted to have a lower reactivity than the 600 °C sample. The higher experimental reactivity may be attributed to volumetric devolatilization steps, which are predominant in not fully pyrolyzed chars with low surface areas as the 550 °C sample. Indeed, although Guizani et al.[13] do not report information on the chars volatile matter, the oxidation behavior of the 550 °C sample exhibits a non-neglible devolatilization step. Indeed, as the 550 °C sample isothermal pyrolysis has 4 s of residence time, it is reasonable to assume that non-negligible amounts of volatile matter are present in the particle. Coupling biomass pyrolysis and char oxidation models is expected to explain the higher experimental reactivity of the 550 °C sample. The present model partly accounts for devolatilization through the low temperature pyrolytic decomposition of $C_2O_2(S)$, but the low specific surface of the sample results in these reactions not accounting for devolatilization phenomena. Considering volumetric bulk devolatilization reactions is expected to explain the reactivity also of biochars with specific surface below the considered threshold (section 2.2).

Figure 9a shows the comparison of oxidation of chars obtained from HTC pyrolysis,[14] where the virgin HTC porosity is obtained from the same study previously considered.[95] The model is less sensitive to the final pyrolysis temperature compared to experimental data due to the high hydrogen content of the 800 °C sample. The importance of the hydrogen to carbon ratio emerges comparing HTC 800 and HTC 5 (the latter is shown in Figure 7). The two samples are subjected to the same operating conditions and are extremely similar except for the hydrogen to carbon weight ratio (9.5×10^{-3} vs 5.2×10^{-3}) and mass specific surface (401 vs 551 $m^2 g^{-1}$) and experimentally exhibit the same reactivity. The higher hydrogen content however corresponds to a higher site density (1.86×10^{-9} vs 1.18×10^{-9} mol cm^{-2}). As the increase in site density is higher than the decrease in surface area, the net result is a predicted higher reactivity of the HTC 800 sample.

Figure 9b shows the comparison of oxidation of biochars obtained from pyrolysis of raw and water leached corn stalk.[82] The authors report only information on virgin and water leached biomasses, therefore char elemental composition and particle porosity were obtained from the biomass pyrolysis model.[11] While the initial porosity was obtained from other studies,[97] the active and unreactive ashes were evaluated from the data reported by the authors on raw and water leached samples, assuming no ash devolatilization occurred. The specific surface area was obtained from the developed correlation (section 2.2). The present comparison allows to validate the coupling of the pyrolysis and oxidation models. The model captures the effect of water leaching and of the different pyrolysis treatments. Moreover, the model reproduces the raw corn stalk chars exhibiting closely resembling reactivities. Although it predicts a higher reactivity for all water leached samples, the main issue is the low reactivity predicted for the char produced at 500 °C. The cause is the low specific surface of 95 $m^2 g^{-1}$, which is below the 100 $m^2 g^{-1}$ threshold value discussed in section 2.2.

5.4. Influence of the Biomass Feedstock Type.

The reactivity of char particles depends also on the type of biomass feedstock. Figure 10 shows the comparison of chars obtained from different biomasses under the same pyrolysis conditions. While Windeatt et al.[80] reported the elemental composition and the specific surface, data on ashes[32,88] and porosity[99−101] were obtained from other sources. The model underestimates of ~50 °C the reactivity of rice husk char and coconut shell. On the contrary, the model overestimates palm shell char oxidation of ~30 °C. The lower reactivity of rice husk is due to the high amount of unreactive ashes ($\omega_{ash}^{p,dry} = 43\%$, $\theta = 0.03$)

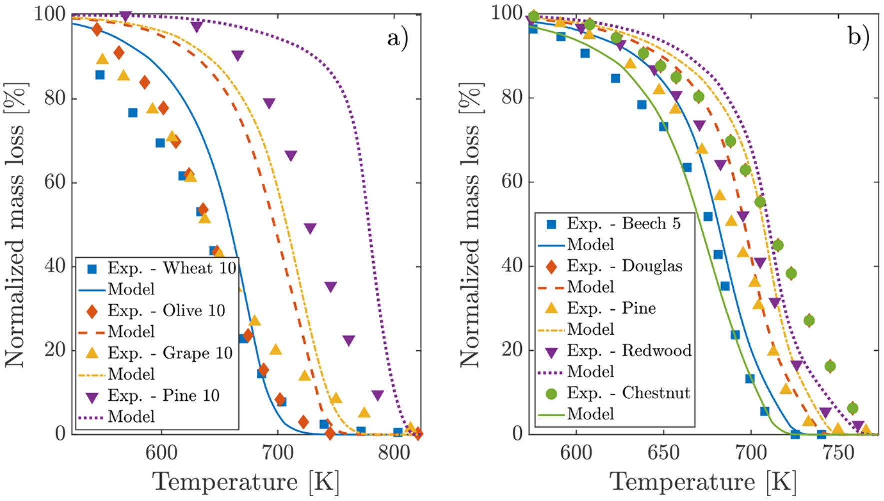

Figure 11. Mass loss in TGA-TPO for chars obtained from different biomasses subjected to the same pyrolysis treatment: (a) experiments of Di Blasi et al.[83] and (b) experiments of Branca and Di Blasi.[87] Comparison between experimental results (marks) and model predictions (lines).

which results in a strong dilution effect. On the other hand, the model predicts palm shell as being more reactive than coconut shell due to the significantly lower carbon content and higher amounts of active ashes of the latter. Furthermore, the elemental compositions reported in ref 80 do not satisfy the mass balances, probably representative of significant uncertainties in the experimental characterization.

Figure 11a shows the same comparison as Figure 10 applied to another set of biomasses.[83] The specific surface was evaluated through the developed correlations (section 2.2). The authors report data on several elements of the ashes composition and were therefore employed in evaluating the reactive ashes. Olive husk porosity was estimated from data on skeletal density,[102] and the same skeletal density was employed to estimate the porosity of grape residues. The porosity of pine wood and wheat straw was obtained from other studies.[103,104] The model is able to describe the difference in reactivity of the chars, although predicting a generally lower reactivity of ~50 °C for all samples except wheat straw. This is partly due to the active ashes being evaluated without considering the presence of iron as it was not measured. The lower reactivity of olive, grape, and pine also relates to their higher carbon content.

Figure 11b shows the oxidation of several wood chars obtained from the same biomass pyrolysis treatment.[87] As for the previous case, the specific surface was obtained from the developed correlations, while the particle porosity was obtained from other studies.[96,104] The porosity of chestnut was evaluated assuming the same skeletal density of beech wood, and the same approach was employed to estimate redwood porosity using pine skeletal density. Ashes composition of the virgin biomass was estimated from other studies on similar biomasses.[32] The present model overestimates the reactivity of the chestnut and fir sample. This is due to the significantly higher amounts of active ashes which enhance considerably char reactivity.

6. CONCLUSION

In this work, a predictive particle-based model coupling physical and chemical descriptions was developed to describe the heterogeneous oxidation of biochar. The biochar particle, described considering both the physical and chemical structures, is fully characterized through its elemental composition and porosity. Additional information such as specific surface and surface site density may also be introduced to further increase the model's reliability. The particle's evolution is described in terms of both physical and chemical phenomena. Consolidated pore models are employed to describe the physical evolution of the particle, while a detailed heterogeneous surface kinetic model was developed to account for the chemical reactivity.

The kinetic model here proposed, which is largely based on previous studies on both char and aromatic clusters oxidation, was extensively validated by means of comparisons with a large amount of experimental data, including conversion rates and product yields. This validation targeted the oxidation of both the same biochar at different operating conditions and different biochars at similar operating conditions. The influences of virgin biomass and type of pyrolysis process on char reactivity have also been successfully explored. Considering the involved uncertainties and the wide range of validation, the model proves able to capture the trends during biochar oxidation, without any case-specific parameter tuning, although significant amounts of information are needed. Additional experimental studies, especially about gas product distribution, are required to further develop the model and to improve its reliability.

However, the current formulation of the model, besides seamlessly integrating physical and chemical phenomena, still lacks the capability to reproduce the oxidation behavior of nonhomogeneous particles in non-kinetically controlled conditions. Coupling of additional phenomena such as intra-particle diffusion, film diffusion, and particle swelling is necessary to further extend the model capabilities and robustness. Similarly, future works will address other important aspects, such as temperature inhomogeneity, heat generation, and heat exchange. Overall, this work constitutes a significant step forward in char pyrolysis and oxidation modeling, and, owing to its general formulation, it may also be applied to describe a broader range of carbonaceous materials, such as graphite, carbon nanotubes, and coal chars.

ASSOCIATED CONTENT

Supporting Information

The Supporting Information is available free of charge at https://pubs.acs.org/doi/10.1021/acs.energyfuels.1c01559.

> Description of particle geometry and mass exchange; in-depth description of the char characterization; correlations to predict skeletal density, mass specific surface and surface site density; complete validation set of the model; sensitivity analysis (PDF)
>
> kinetic.surface: CHEMKIN-like solid-phase reaction mechanism (ZIP)

AUTHOR INFORMATION

Corresponding Author

Tiziano Faravelli − *Department of Chemistry, Materials and Chemical Engineering, Politecnico di Milano, 20133 Milano, Italy*; orcid.org/0000-0001-8382-7342; Email: tiziano.faravelli@polimi.it

Authors

Andrea Locaspi − *Department of Chemistry, Materials and Chemical Engineering, Politecnico di Milano, 20133 Milano, Italy*; orcid.org/0000-0002-4063-8047

Paulo Debiagi − *Department of Mechanical Engineering, Simulation of Reactive Thermo-Fluid Systems, Technical University of Darmstadt, 64287 Darmstadt, Germany*

Matteo Pelucchi − *Department of Chemistry, Materials and Chemical Engineering, Politecnico di Milano, 20133 Milano, Italy*; orcid.org/0000-0003-3106-0236

Christian Hasse − *Department of Mechanical Engineering, Simulation of Reactive Thermo-Fluid Systems, Technical University of Darmstadt, 64287 Darmstadt, Germany*

Complete contact information is available at: https://pubs.acs.org/10.1021/acs.energyfuels.1c01559

Author Contributions

[§]A.L. and P.D. contributed equally to this work.

Notes

The authors declare no competing financial interest.

ACKNOWLEDGMENTS

P.D. and C.H. acknowledge the Deutsche Forschungsgemeinschaft (DFG, German Research Foundation), Project number 215035359 - CRC 129.

NOMENCLATURE

Latin Symbols

$\dot{m}$ = Mass flux [kg s^{-1}]
A = Area [m^2]
a^{ex} = Activity of the exposable mixture [-]
C = Concentration [kmol, m, s]
D_f = Convective Darcy flux [m s^{-1}]
J = Diffusive flux kg [m^{-2} s^{-1}]
K = Particle permeability [m^2]
k = Kinetic constant [mol, cm, s]
k_m = Material transport coefficient [m s^{-1}]
m = Mass [kg]
MW = Molecular weight [g mol^{-1}]
N = Number [-]
n = Number of moles [mol]
P = Pressure [Pa]
R = Molar formation rate [kmol, m, s]
r = Reaction
S = Volumetric specific surface area [m^{2}m^{-3}]
S_g = Mass specific surface area [m^{2}kg^{-1}]
T = Temperature [K]
V = Volume [m^3]
w = Weight of the minimization [-]
x = Species molar fraction [-]
y = Species mass fraction [-]
C(B) = Any bulk carbon
C(S) = Any surface carbon
Ct(B) = Total bulk carbon
Ct(S) = Total surface carbon
G = A generic gas species
Ot(B) = Total bulk oxygenated species
Ot(S) = Total surface oxygenated species
W(B) = A generic bulk species that can be exposed
X(S) = A generic surface species

Greek Letters

α = Consistency parameter [-]
β = Relative amounts of carbonaceous species [-]
χ = Particle mass conversion [-]
δ = Surface site variation [-]
ϵ = Void fraction [-]
η = Reaction order [-]
Γ = Surface site density [kmol m^{-2}]
γ = Particle to system volume ratio [-]
μ = Dynamic viscosity [Pa s]
ν = Stoichiometric coefficient [-]
Ω = Mass formation rate [kg m^{-2}s^{-1}]
ω = Particle mass fraction [-]
ψ = RPM structural parameter [-]
ρ = Density [kg m^{-3}]
$\sigma_{Y/K}$ = Sensitivity coefficient of variable Y to parameter K [-]
θ = Active fraction of inorganic matter [-]
ζ = Deviation of ψ from uniform pore size distribution [-]

Scripts

0 = Initial
co = Bulk exposure reactions consuming surface sites
$diff$ = Diffusive
e = Element e
ext = External
g = Gas
ge = Gas phase in the environment
ha = High reactivity inorganic complexes
i = Species i
in = Inlet
inp = Value used as input for the minimization
j = Reaction j
l = Species l
la = Low reactivity inorganic complexes
ma = Medium reactivity inorganic complexes
n = Normalized
ne = Reactions not involving bulk species exposure
out = Outlet
P = Phase
p = Particle
R = Reactants
r = Reaction
re = Bulk exposure reactions regenerating surface sites
S = Solid
sk = Skeletal

sv = Surface description of volumetric phenomenon
tot = Total
v = Volumetric

REFERENCES

(1) Murty Kanury, A. Thermal decomposition kinetics of wood pyrolysis. *Combust. Flame* **1972**, *18*, 75−83.

(2) Kung, H.-C. A mathematical model of wood pyrolysis. *Combust. Flame* **1972**, *18*, 185−195.

(3) Fan, L. T.; Fan, L.-S.; Miyanami, K.; Chen, T. Y.; Walawender, W. P. A mathematical model for pyrolysis of a solid particle: Effects of the lewis number. *Can. J. Chem. Eng.* **1977**, *55*, 47−53.

(4) Alves, S.; Figueiredo, J. A model for pyrolysis of wet wood. *Chem. Eng. Sci.* **1989**, *44*, 2861−2869.

(5) Larfeldt, J.; Leckner, B.; Melaaen, M. C. Modelling and measurements of heat transfer in charcoal from pyrolysis of large wood particles. *Biomass Bioenergy* **2000**, *18*, 507−514.

(6) Debiagi, P. E. A.; Faravelli, T.; Hasse, C.; Ranzi, E. In *Production of Biofuels and Chemicals with Pyrolysis*; Fang, Z., Smith, R. L., Jr, Xu, L., Eds.; Springer: Singapore, 2020; pp 31−76.

(7) Mayes, H. B.; Broadbelt, L. J. Unraveling the reactions that unravel cellulose. *J. Phys. Chem. A* **2012**, *116*, 7098−7106.

(8) Zhou, X.; Li, W.; Mabon, R.; Broadbelt, L. J. A mechanistic model of fast pyrolysis of hemicellulose. *Energy Environ. Sci.* **2018**, *11*, 1240−1260.

(9) Senneca, O.; Apicella, B.; Russo, C.; Cerciello, F.; Salatino, P.; Heuer, S.; Wütscher, A.; Schiemann, M.; Muhler, M.; Scherer, V. Pyrolysis and Thermal Annealing of Coal and Biomass in CO_2-Rich Atmospheres. *Energy Fuels* **2018**, *32*, 10701−10708.

(10) Weber, K.; Quicker, P. Properties of biochar. *Fuel* **2018**, *217*, 240−261.

(11) Debiagi, P. E. A.; Gentile, G.; Cuoci, A.; Frassoldati, A.; Ranzi, E.; Faravelli, T. A predictive model of biochar formation and characterization. *J. Anal. Appl. Pyrolysis* **2018**, *134*, 326−335.

(12) Neves, D.; Thunman, H.; Matos, A.; Tarelho, L.; Gómez-Barea, A. Characterization and prediction of biomass pyrolysis products. *Prog. Energy Combust. Sci.* **2011**, *37*, 611−630.

(13) Guizani, C.; Jeguirim, M.; Valin, S.; Limousy, L.; Salvador, S. Biomass Chars: The Effects of Pyrolysis Conditions on Their Morphology, Structure, Chemical Properties and Reactivity. *Energies* **2017**, *10*, 796.

(14) Lotz, K.; Wütscher, A.; Düdder, H.; Berger, C. M.; Russo, C.; Mukherjee, K.; Schwaab, G.; Havenith, M.; Muhler, M. Tuning the Properties of Iron-Doped Porous Graphitic Carbon Synthesized by Hydrothermal Carbonization of Cellulose and Subsequent Pyrolysis. *ACS Omega* **2019**, *4*, 4448−4460.

(15) Campbell, P. A.; Mitchell, R. E.; Ma, L. Characterization of coal char and biomass char reactivities to oxygen. *Proc. Combust. Inst.* **2002**, *29*, 519−526.

(16) Tong, W.; Liu, Q.; Ran, G.; Liu, L.; Ren, S.; Chen, L.; Jiang, L. Experiment and expectation: Co-combustion behavior of anthracite and biomass char. *Bioresour. Technol.* **2019**, *280*, 412−420.

(17) Smith, I. W. The combustion rates of coal chars: A review. *Symp. (Int.) Combust., [Proc.]* **1982**, *19*, 1045−1065.

(18) Hurt, R. H.; Calo, J. M. Semi-global intrinsic kinetics for char combustion modeling. *Combust. Flame* **2001**, *125*, 1138−1149.

(19) Hurt, R. H.; Mitchell, R. E. Unified high-temperature char combustion kinetics for a suite of coals of various rank. *Symp. (Int.) Combust., [Proc.]* **1992**, *24*, 1243−1250.

(20) Hong, J.; Hecker, W. C.; Fletcher, T. H. Modeling high-pressure char oxidation using langmuir kinetics with an effectiveness factor. *Proc. Combust. Inst.* **2000**, *28*, 2215−2223.

(21) Su, S.; Song, Y.; Wang, Y.; Li, T.; Hu, S.; Xiang, J.; Li, C. Z. Effects of CO_2 and heating rate on the characteristics of chars prepared in CO_2 and N_2 atmospheres. *Fuel* **2015**, *142*, 243−249.

(22) Tremel, A.; Spliethoff, H. Gasification kinetics during entrained flow gasification – Part II: Intrinsic char reaction rate and surface area development. *Fuel* **2013**, *107*, 653−661.

(23) Holland, T.; Fletcher, T. H. Comprehensive Model of Single Particle Pulverized Coal Combustion Extended to Oxy-Coal Conditions. *Energy Fuels* **2017**, *31*, 2722−2739.

(24) Haynes, B. S.; Newbury, T. G. Oxyreactivity of carbon surface oxides. *Proc. Combust. Inst.* **2000**, *28*, 2197−2203.

(25) Haynes, B. S. A turnover model for carbon reactivity. I. Development. *Combust. Flame* **2001**, *126*, 1421−1432.

(26) Tilghman, M. B.; Mitchell, R. E. Coal and biomass char reactivities in gasification and combustion environments. *Combust. Flame* **2015**, *162*, 3220−3235.

(27) Laurendeau, N. M. Heterogeneous kinetics of coal char gasification and combustion. *Prog. Energy Combust. Sci.* **1978**, *4*, 221−270.

(28) Campbell, P.; Mitchell, R. The impact of the distributions of surface oxides and their migration on characterization of the heterogeneous carbon−oxygen reaction. *Combust. Flame* **2008**, *154*, 47−66.

(29) Su, M.; Tian, X.; Zhao, H. Particle-resolved simulation and modeling of the conversion rate of coal char in chemical looping with oxygen uncoupling. *Combust. Flame* **2020**, *213*, 331−342.

(30) Ranzi, E.; Debiagi, P. E. A.; Frassoldati, A. Mathematical Modeling of Fast Biomass Pyrolysis and Bio-Oil Formation. Note I: Kinetic Mechanism of Biomass Pyrolysis. *ACS Sustainable Chem. Eng.* **2017**, *5*, 2867−2881.

(31) Ranzi, E.; Debiagi, P. E. A.; Frassoldati, A. Mathematical Modeling of Fast Biomass Pyrolysis and Bio-Oil Formation. Note II: Secondary Gas-Phase Reactions and Bio-Oil Formation. *ACS Sustainable Chem. Eng.* **2017**, *5*, 2882−2896.

(32) Vassilev, S. V.; Vassileva, C. G.; Song, Y. C.; Li, W. Y.; Feng, J. Ash contents and ash-forming elements of biomass and their significance for solid biofuel combustion. *Fuel* **2017**, *208*, 377−409.

(33) Maffei, T. Kinetic Model of Coal Combustion. Ph.D. thesis, Politecnico di Milano, 2013.

(34) Keiluweit, M.; Nico, P. S.; Johnson, M.; Kleber, M. Dynamic molecular structure of plant biomass-derived black carbon (biochar). *Environ. Sci. Technol.* **2010**, *44*, 1247−1253.

(35) Bhatia, S. K.; Perlmutter, D. D. A random pore model for fluid-solid reactions: II. Diffusion and transport effects. *AIChE J.* **1981**, *27*, 247−254.

(36) Bhatia, S. K.; Perlmutter, D. D. A random pore model for fluid-solid reactions: I. Isothermal, kinetic control. *AIChE J.* **1980**, *26*, 379−386.

(37) Geng, W.; Nakajima, T.; Takanashi, H.; Ohki, A. Analysis of carboxyl group in coal and coal aromaticity by Fourier transform infrared (FT-IR) spectrometry. *Fuel* **2009**, *88*, 139−144.

(38) Wang, T.; Camps-Arbestain, M.; Hedley, M. Predicting C aromaticity of biochars based on their elemental composition. *Org. Geochem.* **2013**, *62*, 1−6.

(39) Kelemen, S.; Rose, K.; Kwiatek, P. Carbon aromaticity based on XPS Π to Π* signal intensity. *Appl. Surf. Sci.* **1993**, *64*, 167−174.

(40) Bhatia, S. K.; Perlmutter, D. D. The effect of pore structure on fluid-solid reactions: Application to the SO2-lime reaction. *AIChE J.* **1981**, *27*, 226−234.

(41) Pflieger, C.; Lotz, K.; Hilse, N.; Berger, C. M.; Schiemann, M.; Debiagi, P. E. A.; Hasse, C.; Scherer, V.; Muhler, M. Catalytic influence of mineral compounds on the reactivity of cellulose-derived char in O_2-, CO_2-, and H_2O-containing atmospheres. *Fuel* **2021**, *287*, 119584.

(42) Nzihou, A.; Stanmore, B.; Sharrock, P. A review of catalysts for the gasification of biomass char, with some reference to coal. *Energy* **2013**, *58*, 305−317.

(43) Faravelli, T.; Ranzi, E.; Frassoldati, A.; Cuoci, A.; Mehl, M.; Pelucchi, M.; Stagni, A.; Debiagi, P. E. A.; Maffei, L. P.; Nobili, A.; Locaspi, A. *CRECK Modeling, Detailed kinetic mechanisms*; http://creckmodeling.chem.polimi.it/menu-kinetics/menu-kinetics-detailed-mechanisms.

(44) Bagheri, G.; Ranzi, E.; Pelucchi, M.; Parente, A.; Frassoldati, A.; Faravelli, T. Comprehensive kinetic study of combustion technologies

for low environmental impact: MILD and OXY-fuel combustion of methane. *Combust. Flame* **2020**, *212*, 142−155.

(45) Ranzi, E.; Frassoldati, A.; Stagni, A.; Pelucchi, M.; Cuoci, A.; Faravelli, T. Reduced kinetic schemes of complex reaction systems: Fossil and biomass-derived transportation fuels. *Int. J. Chem. Kinet.* **2014**, *46*, 512−542.

(46) Metcalfe, W. K.; Burke, S. M.; Ahmed, S. S.; Curran, H. J. A Hierarchical and Comparative Kinetic Modeling Study of C1 C2 Hydrocarbon and Oxygenated Fuels. *Int. J. Chem. Kinet.* **2013**, *45*, 638−675.

(47) Burke, S. M.; et al. An experimental and modeling study of propene oxidation. Part 2: Ignition delay time and flame speed measurements. *Combust. Flame* **2015**, *162*, 296−314.

(48) Kee, R.; Rupley, F.; Miller, J.; Coltrin, M.; Grcar, J.; Meeks, E.; Mo_at, H.; Lutz, A.; Dixon-Lewis, G.; Smooke, M., et al. *CHEMKIN Release 4.1*; Reaction Design Inc., San Diego, CA, 2006.

(49) Ewing, M. B.; Lilley, T. H.; Olofsson, G. M.; Ratzsch, M. T.; Somsen, G. Standard quantities in chemical thermodynamics. Fugacities, activities and equilibrium constants for pure and mixed phases (IUPAC Recommendations 1994). *Pure Appl. Chem.* **1994**, *66*, 533−552.

(50) Ehrburger, P.; Louys, F.; Lahaye, J. The concept of active sites applied to the study of carbon reactivity. *Carbon* **1989**, *27*, 389−393.

(51) Cuoci, A.; Frassoldati, A.; Faravelli, T.; Ranzi, E. OpenSMOKE ++: An object-oriented framework for the numerical modeling of reactive systems with detailed kinetic mechanisms. *Comput. Phys. Commun.* **2015**, *192*, 237−264.

(52) Singh, R. I.; Mebel, A. M.; Frenklach, M. Oxidation of Graphene-Edge Six- and Five-Member Rings by Molecular Oxygen. *J. Phys. Chem. A* **2015**, *119*, 7528−7547.

(53) Raj, A.; da Silva, G. R.; Chung, S. H. Reaction mechanism for the free-edge oxidation of soot by O_2. *Combust. Flame* **2012**, *159*, 3423−3436.

(54) Chaparala, S. V.; Raj, A. Reaction mechanism for the oxidation of zigzag site on polycyclic aromatic hydrocarbons in soot by O2. *Combust. Flame* **2016**, *165*, 21−33.

(55) Ding, Z.-B.; Di Marco, E.; Pelucchi, M.; Faravelli, T.; Maestri, M. First-principles assessment of the analogy between gas-phase and gas-solid H-abstraction reactions at graphene edges. *Chem. Eng. J.* **2019**, *377*, 119691.

(56) Edwards, D. E.; Zubarev, D. Y.; Lester, W. A.; Frenklach, M. Pathways to soot oxidation: Reaction of oh with phenanthrene radicals. *J. Phys. Chem. A* **2014**, *118*, 8606−8613.

(57) Galimova, G. R.; Azyazov, V. N.; Mebel, A. M. Reaction mechanism, rate constants, and product yields for the oxidation of Cyclopentadienyl and embedded five-member ring radicals with hydroxyl. *Combust. Flame* **2018**, *187*, 147−164.

(58) Zhang, H.; Liu, J.; Wang, X.; Jiang, X. Density functional theory study on two different oxygen enhancement mechanisms during NO-char interaction. *Combust. Flame* **2016**, *169*, 11−18.

(59) You, X.; Wang, H.; Zhang, H. B.; Pilling, M. J. Thermal decomposition of graphene oxyradicals under the influence of an embedded five-membered ring. *Phys. Chem. Chem. Phys.* **2016**, *18*, 12149−12162.

(60) Ma, M.; Brown, T.; Haynes, B. Evaluation of thermal desorption spectra for heterogeneous surfaces: application to carbon surface oxides. *Surf. Sci.* **1993**, *297*, 312−326.

(61) Campbell, P. A. Investigation into the roles of surface oxide complexes and their distributions in the carbon-oxygen heterogeneous reaction mechanism. Ph.D. thesis, Stanford University, 2006.

(62) Tognotti, L.; Longwell, J.; Sarofim, A. The products of the high temperature oxidation of a single char particle in an electrodynamic balance. *Symp. (Int.) Combust., [Proc.]* **1991**, *23*, 1207−1213.

(63) Arthur, J. R. Reactions between carbon and oxygen. *Trans. Faraday Soc.* **1951**, *47*, 164−178.

(64) Guerrero, M.; Ruiz, M. P.; Alzueta, M. U.; Bilbao, R.; Millera, A. Pyrolysis of eucalyptus at different heating rates: Studies of char characterization and oxidative reactivity. *J. Anal. Appl. Pyrolysis* **2005**, *74*, 307−314.

(65) Pratali Maffei, L.; Pelucchi, M.; Faravelli, T.; Cavallotti, C. Theoretical study of sensitive reactions in phenol decomposition. *React. Chem. Eng.* **2020**, *5*, 452−472.

(66) Hurt, R.; Sun, J.-K.; Lunden, M. A Kinetic Model of Carbon Burnout in Pulverized Coal Combustion. *Combust. Flame* **1998**, *113*, 181−197.

(67) Wen, W. Y. Mechanisms of Alkali Metal Catalysis in the Gasification of Coal, Char, or Graphite. *Catal. Rev.: Sci. Eng.* **1980**, *22*, 1−28.

(68) Gallagher, J. T.; Harker, H. Reaction of carbon with oxidizing gases: Catalysis by compounds of iron, cobalt and nickel. *Carbon* **1964**, *2*, 163−173.

(69) Di Blasi, C. Combustion and gasification rates of lignocellulosic chars. *Prog. Energy Combust. Sci.* **2009**, *35*, 121−140.

(70) Wood, B. J.; Fleming, R. H.; Wise, H. Reactive intermediate in the alkali-carbonate-catalysed gasification of coal char. *Fuel* **1984**, *63*, 1600−1603.

(71) Foord, A. D. The carbon-oxygen reaction. Ph.D. thesis, University of Newcastle upon Tyne, 1972.

(72) Du, Z.; Sarofim, A. F.; Longwell, J. P.; Tognotti, L. The CO/CO_2 Ratio in the Products of the Carbon-Oxygen Reaction. *Fundamental Issues in Control of Carbon Gasification Reactivity* **1991**, 91−106.

(73) Otterbein, M.; Bonnetain, L. Combustion d'un carbone vitreux sous basses pressions d'oxygene. *Carbon* **1968**, *6*, 877−885.

(74) Phillips, R.; Vastola, F.; Walker, P. Factors affecting the product ratio of the carbon-oxygen reaction—II. Reaction temperature. *Carbon* **1970**, *8*, 205−210.

(75) Bonnetain, L.; Duval, X.; Letort, M. On the role of surface oxides in the graphite-oxygen reaction. *Carbon*; Elsevier, 1960; pp 107−114.

(76) Rossberg, M. Experimentelle Ergebnisse über die Primärreaktionen bei der Kohlenstoffverbrennung. *Z. Elektrochem., Ber. Bunsenges. Phys. Chem.* **1956**, *60*, 952−956.

(77) Jiang, W.; Nadeau, G.; Zaghib, K.; Kinoshita, K. Thermal analysis of the oxidation of natural graphite — effect of particle size. *Thermochim. Acta* **2000**, *351*, 85−93.

(78) Kim, P.; Johnson, A.; Edmunds, C. W.; Radosevich, M.; Vogt, F.; Rials, T. G.; Labbé, N. Surface functionality and carbon structures in lignocellulosic-derived biochars produced by fast pyrolysis. *Energy Fuels* **2011**, *25*, 4693−4703.

(79) Yu, Y.; Fu, X.; Yu, L.; Liu, R.; Cai, J. Combustion kinetics of pine sawdust biochar: Data smoothing and isoconversional kinetic analysis. *J. Therm. Anal. Calorim.* **2016**, *124*, 1641−1649.

(80) Windeatt, J. H.; Ross, A. B.; Williams, P. T.; Forster, P. M.; Nahil, M. A.; Singh, S. Characteristics of biochars from crop residues: Potential for carbon sequestration and soil amendment. *J. Environ. Manage.* **2014**, *146*, 189−197.

(81) Sun, Y.; Gao, B.; Yao, Y.; Fang, J.; Zhang, M.; Zhou, Y.; Chen, H.; Yang, L. Effects of feedstock type, production method, and pyrolysis temperature on biochar and hydrochar properties. *Chem. Eng. J.* **2014**, *240*, 574−578.

(82) Xu, M.; Sheng, C. Influences of the heat-treatment temperature and inorganic matter on combustion characteristics of cornstalk biochars. *Energy Fuels* **2012**, *26*, 209−218.

(83) Di Blasi, C.; Buonanno, F.; Branca, C. Reactivities of some biomass chars in air. *Carbon* **1999**, *37*, 1227−1238.

(84) Zeng, K.; Minh, D. P.; Gauthier, D.; Weiss-Hortala, E.; Nzihou, A.; Flamant, G. The effect of temperature and heating rate on char properties obtained from solar pyrolysis of beech wood. *Bioresour. Technol.* **2015**, *182*, 114−119.

(85) Dudder, H.; Lotz, K.; Wutscher, A.; Muhler, M. The influence of iron oxide on the oxidation kinetics of synthetic char derived from thermogravimetric analysis and fixed-bed experiments under isothermal and temperature-programmed conditions. *Fuel* **2017**, *201*, 99−104.

(86) Morin, M.; Pécate, S.; Hémati, M.; Kara, Y. Pyrolysis of biomass in a batch fluidized bed reactor: Effect of the pyrolysis conditions and the nature of the biomass on the physicochemical

properties and the reactivity of char. *J. Anal. Appl. Pyrolysis* **2016**, *122*, 511−523.

(87) Branca, C.; Di Blasi, C. Global Kinetics of Wood Char Devolatilization and Combustion. *Energy Fuels* **2003**, *17*, 1609−1615.

(88) Phyllis2, Database for the physico-chemical composition of (treated) lignocellulosic biomass, micro- and macroalgae, various feedstocks for biogas production and biochar; https://phyllis.nl/.

(89) Gentile, G.; Debiagi, P. E. A.; Cuoci, A.; Frassoldati, A.; Ranzi, E.; Faravelli, T. A computational framework for the pyrolysis of anisotropic biomass particles. *Chem. Eng. J.* **2017**, *321*, 458−473.

(90) Entegris, Inc. Graphite Properties and Characteristics; https://poco.entegris.com/content/dam/poco/resources/reference-materials/brochures/brochure-graphite-properties-and-characteristics-11043.pdf.

(91) Burchell, T. In *Comprehensive Nuclear Materials*; Konings, R. J., Ed.; Elsevier: Oxford, 2012; pp 285−305.

(92) Sutton, A.; Howard, V. The role of porosity in the accommodation of thermal expansion in graphite. *J. Nucl. Mater.* **1962**, *7*, 58−71.

(93) Kim, P.; Meyer, H. M.; Agnihotri, S. Effect of Surface Oxygen and Temperature on External and Micropore Adsorption of Water in Single-Walled Carbon Nanotubes by Gravimetric and Spectroscopic Experiments. *J. Phys. Chem. C* **2009**, *113*, 12109−12117.

(94) Yao, N.; Lordi, V.; Ma, S.; Dujardin, E.; Krishnan, A.; Treacy, M.; Ebbesen, T. Structure and oxidation patterns of carbon nanotubes. *J. Mater. Res.* **1998**, *13*, 2432−2437.

(95) Sheng, K.; Zhang, S.; Liu, J.; E, S.; Jin, C.; Xu, Z.; Zhang, X. Hydrothermal carbonization of cellulose and xylan into hydrochars and application on glucose isomerization. *J. Cleaner Prod.* **2019**, *237*, 117831.

(96) Vitas, S.; Segmehl, J.; Burgert, I.; Cabane, E. Porosity and Pore Size Distribution of Native and Delignified Beech Wood Determined by Mercury Intrusion Porosimetry. *Materials* **2019**, *12*, 416.

(97) Zhang, Y.; Ghaly, A. E.; Li, B. Physical properties of corn residues. *Am. J. Biochem. Biotechnol.* **2012**, *8*, 44−53.

(98) Lotz, K.; Berger, C. M.; Muhler, M. Catalytic effect of iron phases on the oxidation of cellulose-derived synthetic char. *Energy Procedia* **2019**, *158*, 694−699.

(99) Guo, J.; Lua, A. C. Characterization of adsorbent prepared from oil-palm shell by CO_2 activation for removal of gaseous pollutants. *Mater. Lett.* **2002**, *55*, 334−339.

(100) Hu, S.; Xiang, J.; Sun, L.; Xu, M.; Qiu, J.; Fu, P. Characterization of char from rapid pyrolysis of rice husk. *Fuel Process. Technol.* **2008**, *89*, 1096−1105.

(101) Zhang, Y.; Ghaly, A. E.; Li, B. Availability and physical properties of residues from major agricultural crops for energy conversion through thermochemical processes. *Am. J. Agric. Biol. Sci.* **2012**, *7*, 312−321.

(102) Gomez-Martin, A.; Chacartegui, R.; Ramirez-Rico, J.; Martinez-Fernandez, J. Performance improvement in olive stone's combustion from a previous carbonization transformation. *Fuel* **2018**, *228*, 254−262.

(103) Zhang, Y.; Ghaly, A. E.; Li, B. Availability and physical properties of residues from major agricultural crops for energy conversion through thermochemical processes. *Am. J. Agric. Biol. Sci.* **2012**, *7*, 312−321.

(104) Usta, I. Comparative Study of Wood Density by Specific Amount of Void Volume (Porosity). *Turkish J. Agric. Forestry* **2003**, *27*, 1−6.